Journal Pre-proof

Optimized artificial intelligence for enhanced ectasia detection using Scheimpflug-based corneal tomography and biomechanical data

Renato Ambrósio Jr , Aydano P. Machado , Edileuza Leão , João Marcelo G. Lyra , Marcella Q. Salomão , Louise G. Pellegrino Esporcatte , João B. R. da Fonseca Filho , Erica Ferreira-Meneses , Nelson B. Sena Jr , Jorge S. Haddad , Alexandre Costa Neto , Gildasio Castelo de Almeida Jr , Cynthia J. Roberts , Ahmed Elsheikh , Riccardo Vinciguerra , Paolo Vinciguerra , Jens Bühren , Thomas Kohnen , Guy M. Kezirian , Farhad Hafezi , Nikki L. Hafezi , Emilio A Torres-Netto , Nanji Lu , David Sung Yong Kang , Omid Kermani , Shizuka Koh , Prema Padmanabhan , Suphi Taneri , William Trattler , Luca Gualdi , José Salgado-Borges , Fernando Faria-Correia , Elias Flockerzi , Berthold Seitz , Vishal Jhanji , Tommy C.Y. Chan , Pedro Manuel Baptista , Dan Z. Reinstein , Timothy J. Archer , Karolinne M. Rocha , George O. Waring IV , Ronald R. Krueger , William J. Dupps , Ramin Khoramnia , Hassan Hashemi , Soheila Asgari , Hamed Momeni-Moghaddam , Siamak Zarei-Ghanavati , Rohit Shetty , Pooja Khamar , Michael W. Belin , Bernardo Lopes , The International Corneal and Ocular and Biomechanics Study Group

PII: S0002-9394(22)00506-2
DOI: https://doi.org/10.1016/j.ajo.2022.12.016
Reference: AJOPHT 12431

To appear in: *American Journal of Ophthalmology*

Received date: December 30, 2021
Revised date: December 11, 2022
Accepted date: December 12, 2022

Please cite this article as: Renato Ambrósio Jr , Aydano P. Machado , Edileuza Leão , João Marcelo G. Lyra , Marcella Q. Salomão , Louise G. Pellegrino Esporcatte , João B. R. da Fonseca Filho , Erica Ferreira-Meneses , Nelson B. Sena Jr , Jorge S. Haddad , Alexandre Costa Neto , Gildasio Castelo de Almeida Jr , Cynthia J. Roberts , Ahmed Elsheikh , Riccardo Vinciguerra , Paolo Vinciguerra , Jens Bühren , Thomas Kohnen , Guy M. Kezirian , Farhad Hafezi , Nikki L. Hafezi , Emilio A Torres-Netto , Nanji Lu , David Sung Yong Kang , Omid Kermani , Shizuka Koh , Prema Padmanabhan , Suphi Taneri , William Trattler , Luca Gualdi , José Salgado-Borges , Fernando Faria-Correia , Elias Flockerzi , Berthold Seitz , Vishal Jhanji , Tommy C.Y. Chan , Pedro Manuel Baptista , Dan Z. Reinstein , Timothy J. Archer , Karolinne M. Rocha , George O. Waring IV , Ronald R. Krueger , William J. Dupps , Ramin Khoramnia , Hassan Hashemi , Soheila Asgari , Hamed Momeni-Moghaddam , Siamak Zarei-Ghanavati , Rohit Shetty , Pooja Khamar , Michael W. Belin , Bernardo Lopes , The International Corneal and Ocular and Biomechanics Study Group, Optimized artificial intelligence

for enhanced ectasia detection using Scheimpflug-based corneal tomography and biomechanical data, *American Journal of Ophthalmology* (2022), doi: https://doi.org/10.1016/j.ajo.2022.12.016

Optimized artificial intelligence for enhanced ectasia detection using Scheimpflug-based corneal tomography and biomechanical data

Renato Ambrósio Jr, MD, PhD[1,2,3,4,5]; Aydano P. Machado, MD, PhD[3,4,5]; Edileuza Leão, PhD[4,6]; João Marcelo G. Lyra, MD, PhD[4,7]; Marcella Q. Salomão, MD[2,3,4]; Louise G. Pellegrino Esporcatte, MD[2,3,4]; João B. R. da Fonseca Filho, MD[1,2]; Erica Ferreira-Meneses, MD[1,2]; Nelson B. Sena Jr, MD[1,2]; Jorge S. Haddad, MD[3]; Alexandre Costa Neto, MD[1,4]; Gildasio Castelo de Almeida Jr, MD, PhD[4]; Cynthia J. Roberts, PhD[8]; Ahmed Elsheikh, PhD[9,10,11]; Riccardo Vinciguerra, MD[9,12]; Paolo Vinciguerra, MD[13,14]; Jens Bühren, MD[15,16]; Thomas Kohnen, MD, PhD, FEBO[16]; Guy M. Kezirian, MD, MBA, FACS[5,17]; Farhad Hafezi, MD, PhD[18,19,20,21,22]; Nikki L. Hafezi, MAS, IP, ETHZ[19,20,23]; Emilio A Torres-Netto, MD, PhD[3,18,19]; Nanji Lu, MD[18,,23,24,25] ; David Sung Yong Kang, MD[26]; Omid Kermani, MD[27]; Shizuka Koh, MD[28];; Prema Padmanabhan, MD[29]; Suphi Taneri, MD[30,31]; William Trattler, MD[32]; Luca Gualdi, MD[33]; José Salgado-Borges, MD, PhD[34]; Fernando Faria-Correia, MD, PhD[35,36]; Elias Flockerzi, MD[37]; Berthold Seitz, MD[37]; Vishal Jhanji, MD[38,39]; Tommy C.Y. Chan, FRCS[,40]; Pedro Manuel Baptista, MD[41]; Dan Z. Reinstein, MD, MA(Cantab), FRCSC, DABO, FRCOphth, FEBO[42,43,44,45]; Timothy J. Archer, MA(Oxon), DipCompSci(Cantab), PhD[42]; Karolinne M. Rocha, MD, PhD[46]; George O. Waring IV, MD[47]; Ronald R. Krueger, MD, MSE[48]; William J. Dupps, MD, PhD[49,50,51]; Ramin Khoramnia, MD, PhD[52], FEBO; Hassan Hashemi, MD[53]; Soheila Asgari, PhD[53]; Hamed Momeni-Moghaddam, PhD[54]; Siamak Zarei-Ghanavati; MD, MSc, FICO[55]; Rohit Shetty, MD, PhD, FRCS [56]; Pooja Khamar, MD[56]; Michael W. Belin, MD[57]; Bernardo Lopes, MD, PhD[2,3,4,9]

– The International Corneal and Ocular and Biomechanics Study Group.

Affiliations:

1. Department of Ophthalmology, the Federal University of the State of Rio de Janeiro; Rio de Janeiro, Brazil.
2. Rio de Janeiro Corneal Tomography and Biomechanics Study Group; Rio de Janeiro, Brazil.
3. Department of Ophthalmology, Federal University of São Paulo; São Paulo, Brazil.
4. Brazilian Artificial Intelligence Networking in Medicine (BrAIN); Maceio and Rio de Janeiro, Brazil.
5. World College of Refractive Surgery & Visual Sciences; Scottsdale, Arizona, USA.
6. Computing Institute, Federal University of Alagoas; Maceio, AL, Brazil.
7. Universidade Estadual de Ciências da Saúde de Alagoas (UNCISAL); Maceio, AL, Brazil.
8. Department of Ophthalmology & Visual Sciences, Department of Biomedical Engineering, The Ohio State University; Columbus, OH, USA.
9. The School of Engineering, University of Liverpool; Liverpool, United Kingdom
10. Beijing Advanced Innovation Center for Biomedical Engineering, Beihang University; Beijing, China.
11. NIHR Biomedical Research Centre for Ophthalmology, Moorfields Eye Hospital NHS Foundation Trust and UCL Institute of Ophthalmology, UK.
12. Humanitas San Pio X Hospital, Milan, Italy.
13. Humanitas University, Department of Biomedical Sciences, Milan, Italy.
14. Humanitas Clinical and Research Center – IRCCS; Rozzano (Mi), Italy.
15. Praxis für Augenheilkunde Prof. Bühren, Frankfurt am Main, Germany

16. Department of Ophthalmology, Goethe Unversity Frankfurt, Frankfurt am Main, Germany
17. SurgiVision® Consultants, Inc.; Scottsdale, Arizona, USA
18. ELZA Institute; Dietikon, Zurich, Switzerland.
19. Light for Sight Foundation; Zurich, Switzerland
20. Center for Applied Biotechnology and Molecular Medicine, University of Zurich, Zurich, Switzerland
21. USC Roski Eye Institute, Miller School of Medicine; Los Angeles, CA, EUA.
22. School of Ophthalmology and Optometry, Wenzhou Medical University; Wenzhou, China.
23. Faculty of Medicine and Health Sciences, University of Antwerp, Wilrijk, Belgium
24. Department of Ophthalmology, Antwerp University Hospital, Edegem, Belgium
25. Emmetropia Mediterranean Eye Institute; Heraklion, Greece.
26. Eyereum Eye Clinic; Seoul, South Korea.
27. Augenklinik am Neumarkt; Cologne, Germany.
28. Department of Ophthalmology, Osaka University Graduate School of Medicine; Osaka, Japan.
29. Department of Cornea and Refractive Surgery, Medical Research Foundation, Sankara Nethralaya; Chennai, Tamil Nadu, India.
30. Center for Refractive Surgery Muenster; Muenster, Germany.
31. University Eye-Clinic, Ruhr-University; Bochum, Germany.
32. Center for Excellence in Eye Care, Miami, FL, USA.
33. Diagnostica Oftalmologica e Microchirurgia Oculare (DOMA), Rome, Italy.
34. Clinica J. Salgado-Borges; Porto, Portugal.

35. Department of Ophthalmology, Hospital de Braga; Braga, Portugal.
36. Life and Health Sciences Research Institute (ICVS), Escola de Medicina, Universidade do Minho; Braga, Portugal.
37. Department of Ophthalmology, Saarland University Medical Center; Homburg, Germany.
38. Department of Ophthalmology and Visual Sciences, The Chinese University of Hong Kong, Hong Kong.
39. Department of Ophthalmology, University of Pittsburgh School of Medicine, Pittsburgh, PA, USA
40. Department of Ophthalmology & Visual Sciences, The Chinese University of Hong Kong; Hong Kong SAR, China.
41. Ophthalmology Department, Centro Hospitalar Universitário do Porto; Porto, Portugal.
42. Reinstein Vision, London Vision Clinic; London United Kingdom.
43. Columbia University Medical Center; New York, New York.
44. Sorbonne Université; Paris, France.
45. Biomedical Science Research Institute, Ulster University; Coleraine, United Kingdom.
46. Storm Eye Institute, Medical University of South Carolina; Charleston, South Carolina, USA.
47. Waring Vision Institute; Mount Pleasant, South Carolina, USA.
48. Stanley M Truhlsen Eye Institute, Department of Ophthalmology and Visual Sciences, University of Nebraska Medical Center, Omaha, , Nebraska, USA.
49. Cole Eye Institute, Cleveland Clinic, Cleveland, Ohio, USA.

50. Department of Biomedical Engineering, Lerner Research Institute, Cleveland, Ohio, USA.
51. Department of Biomedical Engineering, Case Western Reserve University, Cleveland, Ohio, USA.
52. The David J. Apple International Laboratory for Ocular Pathology, Department of Ophthalmology, University of Heidelberg; Heidelberg, Germany.
53. Noor Ophthalmology Research Center, Noor Eye Hospital; Tehran, Iran.
54. Health Promotion Research Center, Zahedan University of Medical Sciences, Zahedan, Iran.
55. Eye Research Center, Mashhad University of Medical Sciences, Mashhad, Iran.
56. Department of Cornea and Refractive Surgery; Narayana Nethralaya, Bangalore, India.
57. Department of Ophthalmology & Vision Science, University of Arizona; Tucson, Arizona, USA.

Corresponding author: Renato Ambrósio Jr, MD, PhD

dr.renatoambrosio@gmail.com; phone/fax +5521 2234-4233

Rua Conde de Bonfim 211/712 – Rio de Janerio, RJ – 20.520-050, Brazil

Financial Disclosure(s): Dr. Ambrósio, Dr. P. Vinciguerra, Dr. R. Vinciguerra, Dr. Roberts, Dr. B. Lopes, Dr. M. Belin, Dr. A. Ahmed, and Dr. J. Bühren are consultants for Oculus Optikgeräte GmbH (Wetzlar, Germany); The remaining authors have no financial disclosures related to this work.

The authors thank Dr. Sven Reisdorf, PhD, Stefanie Berger, and Niklas Schmidt (Oculus Optikgeräte GmbH; Wetzlar, Germany) for their valuable data processing, helpful discussions, and statistical calculations.

This work was partially presented as a paper in the virtual meeting of the ASCRS (American Society of Cataract and Refractive Surgery) 2020.

This article is presented and submitted as an invited thesis for the American Ophthalmological Society by Renato Ambrósio Jr, MD, PhD.

Running head: Optimized Tomography & Biomechanical Index (TBI) for enhanced corneal ectasia

PRECIS

In a multicenter retrospective case-control study, the artificial intelligence algorithm combining parameters from Scheimpflug-based corneal tomography and biomechanical assessments was optimized to further enhance corneal ectasia detection.

Table of Contents – AOS Thesis

ABSTRACT

Purpose: To optimize artificial intelligence (AI) algorithms to integrate Scheimpflug-based corneal tomography and biomechanics to enhance ectasia detection.

Design: Multicenter cross-sectional case-control retrospective study.

Methods: 3,886 unoperated eyes from 3,412 patients had Pentacam and Corvis ST (Oculus Optikgeräte GmbH; Wetzlar, Germany) examinations. The database included one eye randomly selected from 1,680 normal patients (N), and from 1,181 "bilateral" keratoconus (KC) patients, along with 551 normal topography eyes from very asymmetric ectasia patients (VAE-NT), and their 474 unoperated ectatic (VAE-E) eyes. The current TBIv1 (tomographic-biomechanical index) was tested, and an optimized AI algorithm was developed for augmenting accuracy.

Results: The area under the receiver operating characteristic curve (AUC) of the TBIv1 for discriminating clinical ectasia (KC and VAE-E) was 0.999 (98.5% sensitivity; 98.6% specificity [cutoff 0.5]), and for VAE-NT, 0.899 (76% sensitivity; 89.1% specificity [cutoff 0.29]). A novel random forest algorithm (TBIv2), developed with 18 features in 156 trees using 10-fold cross-validation, had significantly higher AUC (0.945; DeLong, p<0.0001) for detecting VAE-NT (84.4% sensitivity and 90.1% specificity; cutoff 0.43; DeLong, p<0.0001), and similar AUC for clinical ectasia (0.999; DeLong, p=0.818; 98.7% sensitivity; 99.2% specificity [cutoff 0.8]). Considering all cases, the TBIv2 had higher AUC (0.985) than TBIv1 (0.974; DeLong, p<0.0001).

Conclusion: AI optimization to integrate Scheimpflug-based corneal tomography and biomechanical assessments augments accuracy for ectasia detection, characterizing ectasia susceptibility in the diverse VAE-NT group. Some VAE patients may be true unilateral ectasia. Machine learning considering additional data, including epithelial thickness or other parameters from multimodal refractive imaging, will continuously enhance accuracy.

INTRODUCTION

Refractive Surgery has stimulated tremendous advances in corneal imaging to enhance safety and predictability of elective and therapeutic procedures. As predicted by Wilson and Klyce in 1991, advances in corneal analysis enable the surgeon to customize refractive corrections and enhance the efficacy to a level that Helmholtz, Placido, and Gullstrand would undoubtedly have been impressed.[1] Nevertheless, the overwhelming data generated determined the need for more efficient ways to analyze the data. Artificial Intelligence (AI), introduced in 1956, has gained increased relevance in ophthalmology with multiple potential applications.[2-6] AI algorithms utilize computer processing power to simulate and augment human interpretation. Such an approach enhances data analysis and the efficiency of clinical decisions by employing a consistent multidimensional assessment of the large volume of information available, such as when assessing data from multimodal corneal and refractive imaging.[7,8]

Maeda, Klyce, and Smolek pioneered the field in describing a neural network (NN) model based on eleven Placido-disk-based topography indices.[9] The automated NN pattern interpretation provided a correct classification for all 108 maps in the training set but correctly classified only 80% (60 out of 75) of the maps in the testing group. While such a difference was statistically significant, the authors discussed the concept of reinforced learning for further refining the model and predicted the paradigm shift related to AI in the field.[9] Since then, AI has made a significant impact on the detection and treatment of keratoconus and ectatic corneal diseases (ECD).[10-24]

The paradigm shift in ECD management was related to introducing crosslinking (CXL) and intrastromal corneal ring segments (ICRS) that could be utilized earlier in the disease process than penetrating keratoplasty.[25,26] These newer treatment modalities highlighted the importance of recognizing mild or subclinical ectatic disease, which is also paramount for identifying patients at risk for iatrogenic ectasia after corneal laser vision correction (LVC).[27] Assessing ectasia risk among elective refractive surgery candidates has evolved to the characterization of the inherent susceptibility of the cornea for biomechanical decompensation and ectasia progression, which lies beyond detecting mild cases with ECD.[28-30] In addition, the ectasia risk assessment should also include the impact of the LVC procedure, which has been heightened by studies involving finite element analysis.[31,32] This concept is in agreement with McGhee's two-hit hypothesis that genetic (intrinsic) and environmental (extrinsic) factors play a role in the etiology of keratoconus,[25] and the biomechanical cycle of decompensation of corneal ectasia proposed by Dupps and Roberts.[33]

Patients presenting with clinical ectasia in one eye but with the contralateral eye with normal anterior curvature (topography) and normal vision have been classically referred to as one of the possible categories of forme fruste keratoconus.[34] While there are no unified criteria to define subclinical keratoconus and forme fruste keratoconus in the literature,[35] such asymmetric cases have been studied using advanced imaging, such as corneal tomography, to demonstrate an improved ability to detect ECD at an early preclinical stage.[7,12,13,17,19,36-39] Such cases are referred to as very asymmetric ectasia (VAE)[17] or highly asymmetric ectasia (HAE).[19] In a study involving cases from Rio de Janeiro (Brazil) and Milan (Italy), the tomographic and biomechanical index (TBI) was developed with AI by applying

random forest with leave-one-out cross-validation (RF/LOOCV). The training set included 94 normal topography eyes from very asymmetric ectasia patients (VAE-NT), along with one eye randomly selected from each of 480 normal patients, one eye randomly selected from 204 "bilateral" keratoconus cases, and the 72 unoperated ectatic eyes (VAE-E). Considering the LOOCV result, the cutoff of 0.79 provided 100% sensitivity and specificity to detect clinical ectasia (KC + VAE-E cases). An adjusted cutoff of 0.29 provided specificity of 96% and 90.4% sensitivity, with an area under the receiver operating characteristic (ROC) curve (AUC) of 0.985.[17]

External validation studies confirmed that the TBI had very high sensitivity and specificity for detecting ECD.[40-47] Some studies, however, found a relatively lower sensitivity for detecting abnormality among eyes considered subclinical keratoconus (SCKC).[48-52] This could be explained by different criteria used to define SCKC,[53] including having normal tomography and biomechanics, based on BAD-D (Belin/Ambrósio Enhanced Ectasia Deviation)[37] and CBI (Corvis Corneal Biomechanical Index).[15] One must consider that some of these supposedly false negatives SCKC cases may truly represent unilateral ectasia patients due to mechanical trauma such as eye rubbing.[54-57] Nevertheless, these findings support the unquestionable need for further enhancing the sensitivity to identify subclinical or mild ectasia cases.

The current study aimed to test if artificial intelligence for integrating Scheimpflug tomography and biomechanical assessments could be upgraded or optimized by machine learning, utilizing a more extensive population data set, thereby providing higher accuracy for ectasia detection.

METHODS

The current multicenter retrospective study followed the 1964 Declaration of Helsinki (revised in 2000). The Institutional Review Board (IRB) and Human Ethics Committee of the Universidade Federal de São Paulo (UNIFESP, SP, Brazil) approved this study.

Participants

The study database comprised three thousand eight hundred and eighty-six unoperated eyes from 3,412 patients. Twenty-five international centers contributed to the data collection. In a similar fashion to work accomplished in the development of the first version of the TBI,[17] the eyes were divided into four groups: normal patients (N), clinical "bilateral" keratoconus (KC) patients, normal topometric (front surface curvature from Pentacam) from very asymmetric ectasia patients (VAE-NT), and the unoperated ectatic (VAE-E) eyes from the VAE patients. One eye was randomly selected from the N and KC groups. Both eyes of the VAE patient entered the study unless the VAE-E eye had undergone any surgery (*n* = 1,680 [N], 1,181[KC], 551[VAE-NT], and 474[VAE-E], respectively)

Every patient had a comprehensive ophthalmic examination, including the Corvis ST and Pentacam HR (Oculus Optikgeräte GmbH; Wetzlar, Germany). As discussed below, only exams with adequate quality for proper analysis were included. Patients were asked to suspend the use of soft contact lens wear for at least one week before the exam, and rigid or hybrid contact lenses were discontinued for a minimum period of three weeks. All cases had the Quad

Refractive Map tomographic data blindly re-evaluated by a fellowship-trained expert (RA) on Cornea and Refractive Surgery to confirm the inclusion criteria.

The inclusion criteria for a normal subject (N) was a clinically unremarkable general eye exam in both eyes, including normal slit-lamp biomicroscopy, distance corrected visual acuity (DCVA) of 20/25 or better, normal Pentacam topometric findings, no previous surgery, and no use of topical medications different than artificial tears in both eyes. The diagnostic criteria for keratoconus (KC) were clinical ectasia in both eyes without previous ocular surgeries.[58,59] The criteria for the diagnosis of corneal ectasia included topometric characteristics, such as skewed asymmetric bow-tie, inferior steepening, and at least one biomicroscopic slit lamp finding (Munson's sign, Vogt's striae, Fleischer's ring, apical thinning, Rizutti's sign).[59] Very asymmetric ectasia (VAE) criteria were the diagnosis of ectasia in one eye based on the prior hitherto described criteria and the fellow eye being clinically normal based on normal biomicroscopy and a relatively normal front surface curvature (Pentacam topometric data).

All measurements with the Corvis ST and Pentacam HR were taken by experienced technicians considering previously reported protocols.[17] Proper exam quality was also assured by a manual, frame-by-frame analysis of each exam, made by an independent masked examiner to ensure the quality of each acquisition. The primary criterion for the Corvis ST measurement was good edge detection over the whole deformation response, excluding alignment errors (x-direction) and blinking errors. Pentacam HR and Corvis ST data were exported to a custom spreadsheet using special software. The Pentacam software version 1.21r59 and Corvis ST software version 1.6b2015 were used to extract an anonymous database containing

340 parameters from rotating Scheimpflug tomography and 90 parameters from the ultra-high-speed Scheimplfug deformation response during non-contact tonometry.

Artificial Intelligence Optimizing Protocol & Statistics

Different software performed statistical analyses and AI development: MedCalc Statistical Software version 16.8.4 (MedCalc, Ostend, Belgium. URL https://www.medcalc.org/), SPSS version 23 (IBM Corp. in Armonk, NY, USA), the R-Core Team version 3.3.1.2016 (R Foundation for Statistical Computing, Vienna, Austria. URL https://www.R-project.org/), a custom-written MATLAB program (R14, The MathWorks, Natick, MA, USA)`, the Orange version 3.21.1 (University of Ljubljana, URL https://orangedatamining.com/), and the Seaborn Python data visualization version 0.11.2 (http://seaborn.pydata.org/).

The data protection procedures included de-identifying the data by a computer server to store and process the data were based on the TRIPOD (transparent reporting of a multivariable prediction model for individual prognosis or diagnosis) recommendations.[60] The data were analyzed and combined utilizing different artificial intelligence (AI) approaches using the "Knowledge Discovery in Databases" methodology.[61] The basic flow of steps for the data mining and the creation of the AI functions is summarized in Figure 1. The process goes from understanding the problem based on previous knowledge, feature selection, and creating different algorithms with cross-validation to validate the models. Then, these AI models are carefully analyzed and further refined to select the final best algorithm.

The first step was data cleaning and preprocessing. The initial data set has 430 attributes, including data related to the exam acquisition. Basic operations removed all irrelevant attributes with more than 40% of the same value, more than 40% of empty values, or with a variance of less than 0.09 among the patients. This step reduced the data set to 219 attributes. Then, the data sets from the original Tomography and Biomechanical Index (TBIv1) study (n=778 patients; 850 eyes),[17] and from the first external validation, including cases from Rio de Janeiro (n=487 patients; 544 eyes)[42] were separated. The remaining 2,474 eyes from 2,147 patients were divided into two subsets training (2/3) and validation (1/3 eyes) for multiple iterations in the next step. Data reduction and projection were performed on training subsets using automatic feature selection techniques, such as forward selection, backward elimination, and genetic algorithms.[62] These methods were applied in a wrapper approach with the following machine learning algorithms: Neural Network with multilayer perceptron (NN/MLP), k-Nearest Neighbors (k-NN), Decision Tree (DT), Logistic Regression Analysis (LRA), and Random Forrest (RF). More than 1,500 different attribute combinations were extracted as the next step considering or not including the TBIv1.

The next phase focused on the models that did not include the TBIv1 and applied those models to the complete data set. At this point, the goal was to build up and rank the predictive models based on the accuracy for ectasia detection. Each selected attribute combination was done using the selected machine learning algorithm. The 10-fold cross-validation was chosen because of the larger population, decreasing computational time and complexity. In this step, 790 predictive models were analyzed and ranked automatically based on the best area under the receiver operating characteristic (ROC) curves (AUC) and sensitivity for detecting VAE-NT

cases. The top fifteen models were selected and carefully analyzed for electing the best five models. Each model was carefully reviewed, considering the clinical relevance of the selected features. Finally, the set of features for each model was tested with different machine learning algorithms to define the best model based on the highest consistency and accuracy.

Statistical Analysis

There were three types of analysis performed: normal versus "disease" (KC + VAE-E + VAE-NT), N versus clinical ectasia (KC + VAE-E), and N versus VAE-NT. First, the Shapiro-Wilk test checked for normal distributions. Considering the distributions of the parameters in the keratoconus group were non-normally distributed, the analyzed parameters were compared among the groups using the nonparametric Kruskal-Wallis test, followed by the post hoc Dunn's test to compare each pair of groups. Statistical significance was determined for a p-value lower than 0.001.

The AUC was calculated for each parameter, considering the best cutoff value for the highest accuracy, determining sensitivity and specificity. Pairwise comparisons of the AUCs were accomplished with a nonparametric approach as described by DeLong and coworkers to compare the performance of diagnostic tests.[63] Separation curves that display accuracy as a function of shifting the cutoff value were plotted as described by Bühren.[11] This method allows for comparisons among the different metrics using normalized cutoff points by a *Z* transformation in which the optimum cutoff is adjusted to zero. The area under the separation curve

(AUSEP) calculates for the *y* limits of 50 and 100% accuracy, separating the *x* limits of -1 and 1 standard deviations. Thus, the separation curves (AUSEP) values indicate the tolerance to shifts on the cutoff criteria, which may evaluate the discriminatory ability of the parameter.[11] For ROC analysis, a custom-written MATLAB program (R14, The MathWorks, Natick, Mass.) was used to confirm results obtained by MedCalc. All combined parameters were programmed to have their output values as a scale value ranging from zero to one. An LRA function was created for the BAD-D to facilitate graphical comparisons.[17]

The correlations between the parameters were tested with Pearson's correlation coefficient (r) or Spearman's coefficient of rank correlation (rho) accordingly to the distribution of the variables.

Results

Table 1 summarizes the age demographics. The mean age in the normal group was 34.2 years old and 31.6 and 31 years old in the KC and VAE groups, respectively. There were significant differences in age (Kruskal-Wallis test, $p<0.001$), with post hoc Dunn's analysis being significant for the differences with normal patients being older than the other groups ($p<0.001$). However, such differences were considered of limited clinical significance, as shown in Figure 2.

The algorithm with the highest accuracy for enhancing ectasia detection was a novel random forest algorithm, called the BrAIN-TBI (Brazilian Artificial Intelligence Networking in Medicine) or TBIv2. The TBIv2 included eighteen features using 156 trees with 10-fold cross-validation. Table 2 summarizes the 18 features selected, including ten parameters from rotating Scheipflug corneal tomography (Pentacam) and eight parameters from corneal deformation response during non-contact tonometry (Corvis ST).

A LRA function was applied for the BAD-D version 3 (Belin/Ambrósio Enhanced Ectasia Deviation [v3]), so that it was normalized as an index, ranging from 0 to 1 (BAD-DI). The BAD-DI was ($y = a + b * x$): -4.02447 (constant) + (2.5203 * BAD-D). The BAD-D and BAD-DI had a perfect correlation (Spearman's coefficient of rank correlation; $p<0.0001$; $rho=1.0$).

Figure 3 illustrates the scatterplot matrices of the most significant parameters plotted pairwisely: age, BAD-D, BAD-DI, PRFI, SPA1, CBI, TBIv1, and TBIv2. Figure 4 presents the box/dot-plot distributions for the most relevant parameters in the four groups.

Tables 3A, 3B, and 3C summarize the AUC data, comparing the accuracy of the TBIv1,[17] the novel TBIv2, the PRFI (Pentacam Random Forest Index),[16] the BAD-D[37] and CBI (Corvis Corneal Biomechanical Index)[15] for N x all (KC+VAE-E+VAE-NT), N x clinical ectasia (KC+VAE-E), and N x VAE-NT. For every pairwise comparison for every analysis, the random forest parameters (TBIv1, TBIv2, and PRFI) had a statistically significant higher AUC than BAD-D and CBI (DeLong, $p<0.001$). In addition, the BAD-D had a higher AUC than CBI for all studies (DeLong, $p<0.001$).

For all cases (N x KC+VAE-E + VAE-NT), the TBIv1 had AUC 0.974, with 90% sensitivity and 96.2% specificity with 0.41 as a cutoff. The AUC of the TBIv1 was 0.999 for discriminating clinical ectasia (KC and VAE-E), having 98.5% sensitivity; 98.6% specificity with a cutoff of 0.5. The AUC of the TBIv1 was 0.899 for VAE-NT, having 76% sensitivity and 89.1% specificity for an optimized cutoff of 0.29. For all cases, the TBIv2 had an AUC of 0.985, with 92.8% sensitivity and 97.4% specificity (cutoff 0.65), which was higher than TBI (0.974; DeLong, $p<0.0001$). The TBIv2 had similar AUC for clinical ectasia (0.999; DeLong, $p=0.818$; 98.7% sensitivity; 99.2% specificity [cutoff 0.8]), but had a higher separation curve. The TBIv2 had significantly higher AUC (0.945; DeLong, $p<0.0001$) for detecting VAE-NT (84.4% sensitivity and 90.1% specificity; cutoff 0.43; DeLong, $p<0.001$). The combination of these 18 features also performed well in a logistic regression analysis (LRA) with AUC 0.984, and a neural network with multilayer perceptron (NN/MLP) including these features had AUC 0.981 for all cases (N x KC+VAE-E + VAE-NT).

The study comparing normal versus all cases or "disease" (KC + VAE-E + VAE-NT) is summarized in Table 3A and Figure 5A. The TBIv2 had a significantly higher AUC than all other parameters (DeLong, $p<0.0001$). The TBIv1 had a larger

AUC (0.974) than PRFI (0.972) but with no statistical significance (DeLong, p=0.2979). The AUSEP curves provided higher separation for the TBIv2, than the TBIv1 and PRFI (87, 82, and 68, respectively)

Table 3B and Figure 5B indicate the study to distinguish N from clinical ectasia cases (KC + VAE-E). The TBIv2, the TBIv1, and the PRFI had a similar AUC of 0.999 and the same 95% confidence intervals between 0.997 to 1. The AUC of the BAD-D was 0.995, which was statistically lower than the TBI and PRFI, but higher than the AUC of the CBI (0.968; DeLong, p<0.0001).

The comparison of normal corneas versus the VAE-NT cases is presented in Table 3C and Figure 5C. In these diverse cases, the difference in accuracy is more pronounced. The TBIv2 had a higher AUC (0.945) than all other parameters (DeLong, p<0.0001). The TBIv1 had a larger AUC (0.899) than PRFI (0.893) but was not statistically significant (DeLong, p=0.299). The AUSEP curves provided higher separation for the TBIv2, than the TBIv1 and PRFI (70, 58, and 36, respectively). The BAD-D had an AUC of 0.823, which was statistically lower than the TBIv1 and PRFI but higher than the AUC of the CBI (0.788; DeLong, p<0.0001). The TBIv1 and TBIv2 had a very high positive correlation with rho of 0.902 (95% Confidence Interval: 0.896 to 0.908; Spearman, p<0.0001; Figure 6).

The Kruskal-Wallis test found statistically significant differences for TBIv1, TBIv2, PRFI, BAD-D, CBI, for maximal axial keratometric value (Kmax), inferior-superior asymmetry value (IS-value), and Ambrósio's relational thickness to the meridian with maximal pachymetric increase (ART-max).[64] There was statistical significance for every parameter at each pairwise group comparison in post hoc

Dunn ($p<0.001$), unless for KC versus VAE-E in any parameter. Table 4 summarizes the descriptive statistics (median and range) for these parameters.

The BAD-D, the best cutoff for distinguishing normal corneas from all groups (KC + VAE-E + VAE-NT) was 1.82, with a sensitivity of 85.5% and a specificity of 97.7%. The BAD-DI cutoff of 0.63 provided similar accuracy. For detecting clinical ectasia (KC + VAE-E), the best cutoff of the BAD-D was 1.98 (BAD-DI of 0.72), with a sensitivity of 96.8% and a specificity of 99.3%. The best cutoff for distinguishing normal and the diverse VAE-NT group was 1.27 (BAD-DI of 0.31) with 70.8% sensitivity and 80.4% specificity. Interestingly, the cutoff of 1.6 (BAD-DI of 0.51), in which the parameter turns yellow in the Belin/Ambrósio Enhanced Ectasia Display, would lead to 94% specificity and 98.4% sensitivity for clinical ectasia, but with a low sensitivity of 52.1% for the VAE-NT cases.

In the original TBIv1 study,[17] objective criteria were rigorously applied for the VAE-NT cases to be considered typical topometric data, including the keratoconus percentage index, KISA%, lower than 60 and a paracentral inferior–superior (I-S value) asymmetry value at 6mm (3mm radii) less than 1.45D.[65] This criterion avoids recognized problems related to subjectivity and inter and intra-examiner inconsistencies for the classifications of topometric maps.[66] While 511 (92.7%) VAE-NT eyes obeyed such criterion, there were forty eyes from this group in the current study with objective topometric abnormalities. These cases were kept in the VAE-NT group as primarily selected subclinical keratoconus (SCKC) because they were confirmed to be very asymmetrical ectasia cases, considering the findings in the fellow VAE-E eye. Interestingly, accordingly to Rabinowitz, these cases are consistent with the criteria for forme fruste keratoconus.[35,67] From the 511 VAE-NT

cases with objectively typical topometric data, 75.1% had TBIv1 higher than 0.29, and 83.3% had TBIv2 higher than 0.43.

The asymmetry of the superior and inferior keratometric values (IS-value) within 6mm, as described by Rabinowitz,[59] with the classical cutoff value of 1.6, would lead to a specificity of 99.6% and a sensitivity of 5.1% for the VAE-NT cases and 84.5% for the clinical ectasia. Reducing the cutoff to 1.45D as the cutoff, the specificity would decrease to 99.3%, with a sensitivity of 86.6% for the clinical ectasia and 6.9% for the VAE-NT cases. The maximal axial keratometric value (Kmax), with a cutoff value of 47.6D would lead to a specificity of 97.7% and a sensitivity of 82.1% for clinical ectasia and 4.9% sensitivity in the VAE-NT cases. Interestingly, 8% of the clinical ectatic patients had a Kmax lower than 46D, and 3.3% had a Kmax lower than 45D. The ART-max,[64] with a cutoff value of 329 microns, has a specificity of 98% and a sensitivity of 93.7% for clinical ectasia but only 34.7% for VAE-NT. If considering the cutoff of 387 microns for ART-max, the specificity would decrease to 83.6%, with a sensitivity of 65.7% for the VAE-NT.

Discussion

The current multicenter cross-sectional case-control retrospective study demonstrated the ability to optimize artificial intelligence (AI) algorithms integrating Scheimpflug-based corneal tomographic and biomechanical data to enhance ectasia detection. AI has the capacity to (and should) continuously evolve, boosting its complexity to improve accuracy.[7,68] AI improvements occur through better training, which necessitates more data for the refinements. The "Knowledge Discovery in Databases" process was applied for data mining and developing AI functions.[61] Feature selection techniques included forward selection, backward elimination, and genetic algorithms.[62] There are two ways to gather more information for the training protocols: larger population data sets and novel attributes or parameters.[2,7,68] We analyzed 3,886 eyes from 3,412 patients, considering 340 parameters extracted from the Pentacam and Corvis ST examinations.

Besides an extensive population data set, including a relatively large set of subclinical cases was a major reason for the success in optimizing AI training in this study. Including such cases allows for identifying nuances in the very mild, asymptomatic cases. In this context, patients presenting with very asymmetric ectasia (VAE), in which the fellow eye had a comprehensive ophthalmic exam within normal limits, have served as the most common models to develop, test, and demonstrate the improved ability to detect ECD by using advanced imaging data.[7,12,13,17,19,36,37,69] Other inclusion criteria that could represent subclinical ectasia cases include the retrospective analysis of the preoperative state of eyes that developed progressive ectasia after laser vision correction procedures,[70] and

longitudinal studies that identify the relatively normal cases with natural ectasia evolution.[55,71,72]

The first version of the TBI training set included 94 VAE-NT eyes, from which 85 (90.4%) had TBIv1 higher than 0.29.[17] The current study included 551 very asymmetric ectasia patients, with 511 within the rigorous, objective criteria for VAE-N: KISA less than 60 and I-S value lower than 1.45D.[65] In this more extensive series of VAE-NT cases, the sensitivity of the TBIv1 for the same cutoff 0.29 was 76%. The new TBIv2 augmented the sensitivity up to 84.4% (DeLong, p<0.0001).

The higher accuracy of the TBIv2 over the TBIv1[17] and the PRFI[16] could not be shown by the ability to detect clinical ectasia. Either TBIv1, TBIv2, and PRFI had a similar AUC of 0.999 with no statistical significance (DeLong, p=0.818). The TBIv2had a slight advantage in accuracy, with 98.7% sensitivity, 99.2% specificity, and a cutoff of 0.8. The TBIv1 had 98.5% sensitivity, 98.6% specificity, and 0.5 as the cutoff. Paradoxically, the AUSEP of the TBIv2 was lower, which may be related to the higher cutoff. Also, while TBIv2 had a higher specificity, more normal cases had higher values (Figure 4). The interpretation for the high TBIv2 scores in some eyes in the clinically normal group is that those cases may have a higher susceptibility to developing ectasia, which can be tested in future prospective studies using finite element simulations.[31] Considering all cases, the TBIv2 also had a higher AUC (0.985) than the TBIv1 (0.974; DeLong, p<0.0001) and PRFI (0.972; DeLong, p<0.0001).

A significant limitation of this study is related to the fact that the VAE cases represent a diverse group because some may be genuine unilateral ectasia cases.[54-57,72,73] According to Global Consensus from 2015, Keratoconus is, by definition, asymmetric bilateral disease, while secondary mechanical-related ectasia may occur

in only one eye. In addition, the 2015 consensus failed to reach an agreement on the definition of *forme fruste* keratoconus (FFKC).[58] Nevertheless, the concept that FFKC remains with high ectasia susceptibility but did not progress to the full-blown presentation of the disease.[74] While there is a significant variability in the criteria for defining subclinical keratoconus and forme fruste keratoconus in the literature, the VAE-NT group may represent a logical group to test the ability of any parameter to quantify the level of predisposition or susceptibility for corneal biomechanical decompensation.[55,69,75] Another limitation of the current study was not to include less common phenotypes of "natural" ectasia: pellucid marginal degeneration, and keratoglobus.[76] Nevertheless, these cases have typical presentations that may facilitate clinical diagnosis, there is a need for future studies testing the accuracy of the novel TBIv2 for detecting such cases.

The BrAIN-TBI or TBIv2 was the most consistent AI algorithm utilizing a novel random forest (RF), including 18 features (Table 2) in 156 trees with 10-fold cross-validation, the most consistent AI algorithm. The parameters that were selected had relatively high clinical relevance. Rotating Scheimpflug tomography (Pentacam) [77,78] provided ten features, and eight parameters were derived from the Corvis ultra-high-speed Scheimpflug imaging during the non-contact tonometry.[79,80] The Pentacam parameters included: the PRFI,[70] the paracentral inferior–superior (IS-value) asymmetry value at 6mm (3mm radii),[65] three metrics from corneal wavefront,[11] one metric from peripheral vertical pachymetric asymmetry,[81,82] the vertical deviation of the Kmax, and two metrics from Belin's enhanced back elevation and one from anterior elevation.[83-85] The CBI,[15] Roberts's stiffness parameters (at first applanation and at highest concavity momentum),[86,87] and other corneal deformation parameters were included.[79,80]

Random forest (RF) is an advanced compound method that involves multiple decision trees. As in a classic decision tree, the analyzed case is successively split into two mutual subgroups (branches) that subdivide until a final decision on class assignment (leaves). The RF approach considers numerous trees for a cooperative effort for the decision output. The algorithm grows the trees by sampling the data into random subgroups. Some input variables are also randomly selected to test the data splitting at each node. According to an objective function, the predictor variable that delivers the best split is applied to each node. Each tree gets a "vote" in the classification process. The final classification is based on the votes of all trees for providing a combined value that typically varies from zero to one.[88]

The consistency of the model is highlighted because both the NN/MLP and LRA algorithms employing the same 18 variables had equally good diagnostic performances. As an iteration process, the RF model with these 18 variables trained with leave-one-out cross-validation (LOOCV) had a slightly better AUC of 0.987 for all cases (N x KC + VAE-E + VAE-NT), but with no statistical significance (DeLong, p=0.169). As for any machine learning method, it is fundamental to include a cross-validation method to minimize the risk of overfitting. Proper cross-validation will infer or presume the ability to generalize the external validity of the model. The first version of the TBI utilized LOOCV.[17] In contrast, the current study employed ten-fold cross-validation because of the larger population as it decreases computational time and complexity, still maintaining and possibly enhancing generalization. By this means, the 10-fold cross-validation ensures the reliability or robustness of the model for classifying new data. Unlike LOOCV, the database is randomly divided into ten groups, balancing the number of cases in the subgroups. Subsequently, the AI training of the model has repeated ten folds. Each time, one group is excluded, in

which the model trained with the 9/10 cases is tested. The reported outcomes of the TBIv2 include the outputs from the 10-fold cross-validation model. These results present a lower (less optimistic) accuracy when compared to the virtually perfect accuracy of the final TBIv2 model that contemplates all cases and will be programmed in the commercial Oculus software (Ambrósio, Roberts & Vinciguerra Tomography and Biomechanical Display). However, the cross-validation results are expected to represent a more trustworthy picture of the expected generalized performance for the TBIv2 in clinical application.

The last three decades witnessed a tremendous advance in corneal imaging, which includes the development of high-resolution technologies capable of detailed characterizations of different aspects of corneal shape and anatomy and introducing scientifically validated methods for representing and interpreting the generated data.[89] Applying AI was a natural progression for analyzing the overwhelming plethora of available data.[7,8,54]

Placido-disk-based corneal topography characterizes the anterior or front corneal surface, enabling the detection of abnormalities consistent with mild to moderate forms of keratoconus in eyes with normal slit-lamp biomicroscopy and normal distance corrected visual acuity.[90,91] There are still cases that develop ectasia despite relatively normal preoperative topography prior to LASIK,[30,92-94] SmILE (small incision lenticular extraction),[95,96] surface ablation,[97] and even LASIK-Xtra (LASIK with prophylactic crosslinking).[98] Ectasia detection is also relevant when evaluating candidates for refractive cataract surgery,[99] because it impacts IOL calculation, quality of vision, and the ability for corneal enhancements.[100,101]

Front surface corneal topography evolved into three-dimension (3D) tomographic analysis, which characterizes the front (including topometric or curvature) and back surfaces' elevation and thickness mapping.[102] Further advances in corneal imaging allowed for segmental or layered tomographic (3D) characterization with epithelial thickness,[14,103-105] and Bowman's layer mapping.[20,106,107] Beyond shape analysis, in the context of multimodal refractive imaging,[8] clinical biomechanical assessment has been considered an additional tool for augmenting the sensitivity for identifying mild forms of ECD and the characterization of the inherent susceptibility for ectasia progression.[17,53,108,109] Future biomechanical assessment to characterize material stiffness using Corvis ST data (i.e., Stress-Strain Index [SSI] map),[110] or from novel tools such as Brillouin microscopy,[111-115] and phase-decorrelation ocular coherence tomography (PhD-OCT)[111,116-118] may further enhance AI applications. Ultimately, genetic testing through linkage analysis or genome-wide association studies may further elucidate about the intrinsic susceptibility for biomechanical decompensation, which promises to test and further improve AI for ectasia diagnosis.[119-121]

This study was limited to patients with unoperated corneas. Future external validation studies are needed to test the accuracy of the TBIv2, including testing the specificity among cases with high astigmatism, corneal warpage and dry eye. Further AI optimization is expected for post-laser vision correction procedures, as developed by Vinciguerra and coworkers for the CBI-post LVC.[122] In addition, specific improvements for certain ethnicities (i.e., Chinese and Sub-Saharan Africa) can augment specificity while not jeopardizing the model's sensitivity. Besides diagnosis, AI can be developed to improve prognosis and clinical follow-up, as described by integrating biomechanical parameters into Belin's tomographic ABCD

system.[123-125] The relevance for enhanced ectasia detection may go beyond the management of ECD cases and assessing ectasia risk prior to elective laser vision correction procedures. For example, there are different associations of keratoconus with posterior segment structures findings (i.e., optic nerve head and the choroid).[126] In addition, the hypothesis that mild or subclinical keratoconus could be a risk factor for a mother to have a baby with Down's syndrome was also raised.[127] While understanding the underlying mechanisms for such relationships is not complete, enhanced analysis of the cornea based on properly trained AI, considering specific well-designed fundamental questions, may provide relevant parameters for future clinical applications.

The current study validated the hypothesis that AI can be optimized to improve ectasia detection. Such advances may augment the reliability of clinical decisions related to screening cases at risk for ectasia after LVC. The relevance of AI develops fast in different areas of Ophthalmology. We predict rapid developments with increasing applications for enhancing the safety and efficiency of therapeutic and elective Refractive Surgery. AI advances should involve gathering extensive data from large populations and including features from multimodal imaging technologies, such as epithelial thickness (segmental or layered tomography), axial length, and ocular wavefront data.

References

1. Wilson SE, Klyce SD. Advances in the analysis of corneal topography. *Surv Ophthalmol.* 1991;35(4):269-277.
2. Kapoor R, Walters SP, Al-Aswad LA. The current state of artificial intelligence in ophthalmology. *Surv Ophthalmol.* 2019;64(2):233-240.
3. Abramoff MD, Tobey D, Char DS. Lessons Learned About Autonomous AI: Finding a Safe, Efficacious, and Ethical Path Through the Development Process. *Am J Ophthalmol.* 2020;214:134-142.
4. Chiang M, Guth D, Pardeshi AA, et al. Glaucoma Expert-Level Detection of Angle Closure in Goniophotographs With Convolutional Neural Networks: The Chinese American Eye Study. *Am J Ophthalmol.* 2021;226:100-107.
5. Cheng H, Wang L, Kane JX, Li J, Liu L, Wu M. Accuracy of Artificial Intelligence Formulas and Axial Length Adjustments for Highly Myopic Eyes. *Am J Ophthalmol.* 2021;223:100-107.
6. Keenan TDL, Chakravarthy U, Loewenstein A, Chew EY, Schmidt-Erfurth U. Automated Quantitative Assessment of Retinal Fluid Volumes as Important Biomarkers in Neovascular Age-Related Macular Degeneration. *Am J Ophthalmol.* 2021;224:267-281.
7. Lopes BT, Eliasy A, Ambrosio R. Artificial intelligence in corneal diagnosis: where are we? *Current Ophthalmology Reports.* 2019;7(3):204-211.
8. Ambrosio R, Jr. Multimodal imaging for refractive surgery: Quo vadis? *Indian J Ophthalmol.* 2020;68(12):2647-2649.
9. Maeda N, Klyce SD, Smolek MK. Neural network classification of corneal topography. Preliminary demonstration. *Invest Ophthalmol Vis Sci.* 1995;36(7):1327-1335.
10. Smolek MK, Klyce SD. Current keratoconus detection methods compared with a neural network approach. *Invest Ophthalmol Vis Sci.* 1997;38(11):2290-2299.
11. Buhren J, Kuhne C, Kohnen T. Defining subclinical keratoconus using corneal first-surface higher-order aberrations. *Am J Ophthalmol.* 2007;143(3):381-389.
12. Arbelaez MC, Versaci F, Vestri G, Barboni P, Savini G. Use of a support vector machine for keratoconus and subclinical keratoconus detection by topographic and tomographic data. *Ophthalmology.* 2012;119(11):2231-2238.
13. Smadja D, Touboul D, Cohen A, et al. Detection of subclinical keratoconus using an automated decision tree classification. *Am J Ophthalmol.* 2013;156(2):237-246 e231.
14. Silverman RH, Urs R, Roychoudhury A, Archer TJ, Gobbe M, Reinstein DZ. Epithelial remodeling as basis for machine-based identification of keratoconus. *Invest Ophthalmol Vis Sci.* 2014;55(3):1580-1587.
15. Vinciguerra R, Ambrósio Jr R, Elsheikh A, et al. Detection of keratoconus with a new biomechanical index. *Journal of refractive surgery.* 2016;32(12):803-810.
16. Lopes BT, Ramos IC, Salomao MQ, et al. Enhanced Tomographic Assessment to Detect Corneal Ectasia Based on Artificial Intelligence. *Am J Ophthalmol.* 2018;195:223-232.
17. Ambrosio R, Jr., Lopes BT, Faria-Correia F, et al. Integration of Scheimpflug-Based Corneal Tomography and Biomechanical Assessments for Enhancing Ectasia Detection. *J Refract Surg.* 2017;33(7):434-443.
18. Klyce SD. The Future of Keratoconus Screening with Artificial Intelligence. *Ophthalmology.* 2018;125(12):1872-1873.
19. Hwang ES, Perez-Straziota CE, Kim SW, Santhiago MR, Randleman JB. Distinguishing Highly Asymmetric Keratoconus Eyes Using Combined Scheimpflug and Spectral-Domain OCT Analysis. *Ophthalmology.* 2018;125(12):1862-1871.
20. Chandapura R, Salomao MQ, Ambrosio R, Jr., Swarup R, Shetty R, Sinha Roy A. Bowman's topography for improved detection of early ectasia. *J Biophotonics.* 2019;12(10):e201900126.

21. Maile H, Li JO, Gore D, et al. Machine Learning Algorithms to Detect Subclinical Keratoconus: Systematic Review. *JMIR Med Inform.* 2021;9(12):e27363.
22. Kanellopoulos AJ. Keratoconus Management With Customized Photorefractive Keratectomy by Artificial Intelligence Ray-Tracing Optimization Combined With Higher Fluence Corneal Crosslinking: The Ray-Tracing Athens Protocol. *Cornea.* 2021;40(9):1181-1187.
23. Atalay E, Ozalp O, Yildirim N. Advances in the diagnosis and treatment of keratoconus. *Ther Adv Ophthalmol.* 2021;13:25158414211012796.
24. Malyugin B, Sakhnov S, Izmailova S, et al. Keratoconus Diagnostic and Treatment Algorithms Based on Machine-Learning Methods. *Diagnostics (Basel).* 2021;11(10).
25. McGhee CN, Kim BZ, Wilson PJ. Contemporary Treatment Paradigms in Keratoconus. *Cornea.* 2015;34 Suppl 10:S16-23.
26. Ambrósio R, Lopes B, Amaral J, et al. Keratoconus: Breaking paradigms and contradictions of a new subspecialty. Vol 78: Sociedade Brasileira de Oftalmologia; 2019:81-85.
27. Binder PS, Lindstrom RL, Stulting RD, et al. Keratoconus and corneal ectasia after LASIK. *J Refract Surg.* 2005;21(6):749-752.
28. Ambrosio R, Jr., Randleman JB. Screening for ectasia risk: what are we screening for and how should we screen for it? *J Refract Surg.* 2013;29(4):230-232.
29. Ambrósio Jr R, Belin M. Enhanced screening for ectasia risk prior to laser vision correction. *Int J Keratoconus Ectatic Corneal Dis.* 2017;6(1):23-33.
30. Ambrósio Jr R. Post-LASIK ectasia: twenty years of a conundrum. Paper presented at: Seminars in ophthalmology2019.
31. Dupps WJ, Jr., Seven I. A Large-Scale Computational Analysis of Corneal Structural Response and Ectasia Risk in Myopic Laser Refractive Surgery. *Trans Am Ophthalmol Soc.* 2016;114:T1.
32. Francis M, Khamar P, Shetty R, et al. In Vivo Prediction of Air-Puff Induced Corneal Deformation Using LASIK, SMILE, and PRK Finite Element Simulations. *Invest Ophthalmol Vis Sci.* 2018;59(13):5320-5328.
33. Roberts CJ, Dupps WJ, Jr. Biomechanics of corneal ectasia and biomechanical treatments. *J Cataract Refract Surg.* 2014;40(6):991-998.
34. Klyce SD. Chasing the suspect: keratoconus. *Br J Ophthalmol.* 2009;93(7):845-847.
35. Henriquez MA, Hadid M, Izquierdo L, Jr. A Systematic Review of Subclinical Keratoconus and Forme Fruste Keratoconus. *J Refract Surg.* 2020;36(4):270-279.
36. Saad A, Gatinel D. Topographic and tomographic properties of forme fruste keratoconus corneas. *Invest Ophthalmol Vis Sci.* 2010;51(11):5546-5555.
37. Ambrosio R, Jr., Valbon BF, Faria-Correia F, Ramos I, Luz A. Scheimpflug imaging for laser refractive surgery. *Curr Opin Ophthalmol.* 2013;24(4):310-320.
38. Golan O, Piccinini AL, Hwang ES, et al. Distinguishing Highly Asymmetric Keratoconus Eyes Using Dual Scheimpflug/Placido Analysis. *Am J Ophthalmol.* 2019;201:46-53.
39. Mahmoud AM, Nunez MX, Blanco C, et al. Expanding the cone location and magnitude index to include corneal thickness and posterior surface information for the detection of keratoconus. *Am J Ophthalmol.* 2013;156(6):1102-1111.
40. Sedaghat M-R, Momeni-Moghaddam H, Ambrósio Jr R, et al. Diagnostic ability of corneal shape and biomechanical parameters for detecting frank keratoconus. *Cornea.* 2018;37(8):1025-1034.
41. Kataria P, Padmanabhan P, Gopalakrishnan A, Padmanaban V, Mahadik S, Ambrósio Jr R. Accuracy of Scheimpflug-derived corneal biomechanical and tomographic indices for detecting subclinical and mild keratectasia in a South Asian population. *Journal of Cataract & Refractive Surgery.* 2019;45(3):328-336.
42. Ferreira-Mendes J, Lopes BT, Faria-Correia F, Salomão MQ, Rodrigues-Barros S, Ambrósio Jr R. Enhanced ectasia detection using corneal tomography and biomechanics. *American journal of ophthalmology.* 2019;197:7-16.

43. Salomao MQ, Hofling-Lima AL, Gomes Esporcatte LP, et al. The Role of Corneal Biomechanics for the Evaluation of Ectasia Patients. *Int J Environ Res Public Health.* 2020;17(6).
44. Fernandez J, Rodriguez-Vallejo M, Pinero DP. Tomographic and Biomechanical Index (TBI) for Screening in Laser Refractive Surgery. *J Refract Surg.* 2019;35(6):398.
45. Liu Y, Zhang Y, Chen Y. Application of a scheimpflug-based biomechanical analyser and tomography in the early detection of subclinical keratoconus in chinese patients. *BMC Ophthalmol.* 2021;21(1):339.
46. Zhang M, Zhang F, Li Y, Song Y, Wang Z. Early Diagnosis of Keratoconus in Chinese Myopic Eyes by Combining Corvis ST with Pentacam. *Curr Eye Res.* 2020;45(2):118-123.
47. Augustin VA, Son HS, Baur I, Zhao L, Auffarth GU, Khoramnia R. Detecting subclinical keratoconus by biomechanical analysis in tomographically regular keratoconus fellow eyes. *Eur J Ophthalmol.* 2021:11206721211063740.
48. Steinberg J, Siebert M, Katz T, et al. Tomographic and Biomechanical Scheimpflug Imaging for Keratoconus Characterization: A Validation of Current Indices. *J Refract Surg.* 2018;34(12):840-847.
49. Chan TCY, Wang YM, Yu M, Jhanji V. Comparison of Corneal Tomography and a New Combined Tomographic Biomechanical Index in Subclinical Keratoconus. *J Refract Surg.* 2018;34(9):616-621.
50. Koh S, Ambrosio R, Jr., Inoue R, Maeda N, Miki A, Nishida K. Detection of Subclinical Corneal Ectasia Using Corneal Tomographic and Biomechanical Assessments in a Japanese Population. *J Refract Surg.* 2019;35(6):383-390.
51. Koc M, Aydemir E, Tekin K, Inanc M, Kosekahya P, Kiziltoprak H. Biomechanical Analysis of Subclinical Keratoconus With Normal Topographic, Topometric, and Tomographic Findings. *Journal of Refractive Surgery.* 2019;35(4):247-252.
52. Fraenkel D, Hamon L, Daas L, et al. Tomographically normal partner eye in very asymmetrical corneal ectasia: biomechanical analysis. *J Cataract Refract Surg.* 2021;47(3):366-372.
53. Esporcatte LPG, Salomão MQ, Lopes BT, et al. Biomechanical diagnostics of the cornea. *Eye and Vision.* 2020;7(1):1-12.
54. Salomão M, Hoffling-Lima AL, Lopes B, et al. Recent developments in keratoconus diagnosis. *Expert Review of Ophthalmology.* 2018;13(6):329-341.
55. Salomão MQ, Hofling-Lima AL, Esporcatte LPG, et al. Ectatic diseases. *Experimental Eye Research.* 2021;202:108347.
56. Kansal V, Ambrósio Jr R, Sharma V. Unilateral Traumatic Posterior Corneal Ectasia: Clinical Manifestations, Findings of Advanced Imaging, and Long-term Follow-up. *Journal of Refractive Surgery Case Reports.* 2021;1(3):e31-e35.
57. Criado GG, Júnior NBS, Mazzeo TJMM, et al. Caracterização de ectasia subclínica com análise integrada da tomografia e biomecânica da córnea. 2021;80(1):71-76.
58. Gomes JA, Tan D, Rapuano CJ, et al. Global consensus on keratoconus and ectatic diseases. *Cornea.* 2015;34(4):359-369.
59. Rabinowitz YS. Keratoconus. *Surv Ophthalmol.* 1998;42(4):297-319.
60. Collins GS, Reitsma JB, Altman DG, Moons KG. Transparent reporting of a multivariable prediction model for individual prognosis or diagnosis (TRIPOD): the TRIPOD Statement. *BMC Med.* 2015;13:1.
61. Fayyad U, Piatetsky-Shapiro G, Smyth P. From Data Mining to Knowledge Discovery in Databases. *AI Magazine.* 1996;17(3):37.
62. Khalid S, Khalil T, Nasreen S. A survey of feature selection and feature extraction techniques in machine learning. Paper presented at: 2014 Science and Information Conference; 27-29 Aug. 2014, 2014.
63. DeLong ER, DeLong DM, Clarke-Pearson DL. Comparing the areas under two or more correlated receiver operating characteristic curves: a nonparametric approach. *Biometrics.* 1988;44(3):837-845.

64. Ambrosio R, Jr., Caiado AL, Guerra FP, et al. Novel pachymetric parameters based on corneal tomography for diagnosing keratoconus. *J Refract Surg.* 2011;27(10):753-758.
65. Rabinowitz YS, Rasheed K. KISA% index: a quantitative videokeratography algorithm embodying minimal topographic criteria for diagnosing keratoconus. *J Cataract Refract Surg.* 1999;25(10):1327-1335.
66. Ramos IC, Correa R, Guerra FP, et al. Variability of subjective classifications of corneal topography maps from LASIK candidates. *J Refract Surg.* 2013;29(11):770-775.
67. Rabinowitz YS, Li X, Canedo AL, Ambrosio R, Jr., Bykhovskaya Y. Optical coherence tomography combined with videokeratography to differentiate mild keratoconus subtypes. *J Refract Surg.* 2014;30(2):80-87.
68. Benke K, Benke G. Artificial Intelligence and Big Data in Public Health. *Int J Environ Res Public Health.* 2018;15(12).
69. Luz A, Lopes B, Hallahan KM, et al. Enhanced Combined Tomography and Biomechanics Data for Distinguishing Forme Fruste Keratoconus. *J Refract Surg.* 2016;32(7):479-494.
70. Lopes BT, Ramos IC, Salomão MQ, et al. Enhanced tomographic assessment to detect corneal ectasia based on artificial intelligence. *American journal of ophthalmology.* 2018;195:223-232.
71. Kosekahya P, Koc M, Caglayan M, Kiziltoprak H, Tekin K, Atilgan CU. Longitudinal corneal tomographical changes in eyes of patients with unilateral and bilateral non-progressive keratoconus. *Cont Lens Anterior Eye.* 2019;42(4):434-438.
72. Imbornoni LM, Padmanabhan P, Belin MW, Deepa M. Long-Term Tomographic Evaluation of Unilateral Keratoconus. *Cornea.* 2017;36(11):1316-1324.
73. Ambrósio R, Faria-Correia F, Ramos I, et al. Enhanced screening for ectasia susceptibility among refractive candidates: the role of corneal tomography and biomechanics. *Current Ophthalmology Reports.* 2013;1(1):28-38.
74. Koh S, Ambrósio Jr R, Maeda N, Nishida K. Evidence of corneal ectasia susceptibility: a new definition of forme fruste keratoconus. *Journal of Cataract & Refractive Surgery.* 2020;46(11):1570-1572.
75. Vinciguerra R, Ambrosio R, Jr., Roberts CJ, Azzolini C, Vinciguerra P. Biomechanical Characterization of Subclinical Keratoconus Without Topographic or Tomographic Abnormalities. *J Refract Surg.* 2017;33(6):399-407.
76. Krachmer JH, Feder RS, Belin MW. Keratoconus and related noninflammatory corneal thinning disorders. *Surv Ophthalmol.* 1984;28(4):293-322.
77. Belin MW, Ambrósio Jr R. Scheimpflug imaging for keratoconus and ectatic disease. *Indian journal of ophthalmology.* 2013;61(8):401.
78. Ambrósio R, Valbon BF, Faria-Correia F, Ramos I, Luz A. Scheimpflug imaging for laser refractive surgery. *Current opinion in ophthalmology.* 2013;24(4):310-320.
79. Ambrósio Jr R, Ramos I, Luz A, et al. Dynamic ultra high speed Scheimpflug imaging for assessing corneal biomechanical properties. *Revista Brasileira de Oftalmologia.* 2013;72:99-102.
80. Salomão MQ, Hofling-Lima AL, Faria-Correia F, et al. Dynamic corneal deformation response and integrated corneal tomography. *Indian journal of ophthalmology.* 2018;66(3):373.
81. Ambrósio Jr R. Percentage Thickness Increase and Absolute Difference from Thinnest to Describe Thickness Profile To the Editor. *Journal of Refractive Surgery.* 2009;25(9).
82. Ambrósio Jr R, Alonso RS, Luz A, Velarde LGC. Corneal-thickness spatial profile and corneal-volume distribution: tomographic indices to detect keratoconus. *Journal of Cataract & Refractive Surgery.* 2006;32(11):1851-1859.
83. Belin MW, Khachikian SS. An introduction to understanding elevation-based topography: how elevation data are displayed - a review. *Clin Exp Ophthalmol.* 2009;37(1):14-29.

84. Feng MT, Belin MW, Ambrosio R, Jr., et al. International values of corneal elevation in normal subjects by rotating Scheimpflug camera. *J Cataract Refract Surg.* 2011;37(10):1817-1821.
85. Gilani F, Cortese M, Ambrosio RR, Jr., et al. Comprehensive anterior segment normal values generated by rotating Scheimpflug tomography. *J Cataract Refract Surg.* 2013;39(11):1707-1712.
86. Roberts CJ, Mahmoud AM, Bons J, et al. A new stiffness parameter in air puff induced corneal deformation analysis. *Investigative Ophthalmology & Visual Science.* 2016;57(12).
87. Roberts CJ, Mahmoud AM, Bons JP, et al. Introduction of two novel stiffness parameters and interpretation of air Puff–Induced biomechanical deformation parameters with a dynamic scheimpflug analyzer. *Journal of refractive surgery.* 2017;33(4):266-273.
88. Breiman L. Random Forests. *Machine Learning.* 2001;45(1):5-32.
89. Salomao MQ, Esposito A, Dupps WJ, Jr. Advances in anterior segment imaging and analysis. *Curr Opin Ophthalmol.* 2009;20(4):324-332.
90. Wilson SE, Ambrosio R. Computerized corneal topography and its importance to wavefront technology. *Cornea.* 2001;20(5):441-454.
91. Ambrosio R, Jr., Klyce SD, Wilson SE. Corneal topographic and pachymetric screening of keratorefractive patients. *J Refract Surg.* 2003;19(1):24-29.
92. Klein SR, Epstein RJ, Randleman JB, Stulting RD. Corneal ectasia after laser in situ keratomileusis in patients without apparent preoperative risk factors. *Cornea.* 2006;25(4):388-403.
93. Chan CC, Hodge C, Sutton G. External analysis of the Randleman Ectasia Risk Factor Score System: a review of 36 cases of post LASIK ectasia. *Clin Experiment Ophthalmol.* 2010;38(4):335-340.
94. Bohac M, Koncarevic M, Pasalic A, et al. Incidence and Clinical Characteristics of Post LASIK Ectasia: A Review of over 30,000 LASIK Cases. *Semin Ophthalmol.* 2018;33(7-8):869-877.
95. Shetty R, Kumar NR, Khamar P, et al. Bilaterally Asymmetric Corneal Ectasia Following SMILE With Asymmetrically Reduced Stromal Molecular Markers. *J Refract Surg.* 2019;35(1):6-14.
96. Moshirfar M, Tukan AN, Bundogji N, et al. Ectasia After Corneal Refractive Surgery: A Systematic Review. *Ophthalmol Ther.* 2021;10(4):753-776.
97. Malecaze F, Coullet J, Calvas P, Fournie P, Arne JL, Brodaty C. Corneal ectasia after photorefractive keratectomy for low myopia. *Ophthalmology.* 2006;113(5):742-746.
98. Taneri S, Kiessler S, Rost A, Dick HB. Corneal Ectasia After LASIK Combined With Prophylactic Corneal Cross-linking. *J Refract Surg.* 2017;33(1):50-52.
99. Maeno S, Koh S, Ambrosio R, Jr., Nishida K. Underestimated corneal abnormalities prior to cataract surgery in university hospital settings. *J Cataract Refract Surg.* 2021;47(4):547-548.
100. Vastardis I, Sagri D, Fili S, Wolfelschneider P, Kohlhaas M. Current Trends in Modern Visual Intraocular Lens Enhancement Surgery in Stable Keratoconus: A Synopsis of Do's, Don'ts and Pitfalls. *Ophthalmol Ther.* 2019;8(Suppl 1):33-47.
101. Wang KM, Jun AS, Ladas JG, Siddiqui AA, Woreta F, Srikumaran D. Accuracy of Intraocular Lens Formulas in Eyes With Keratoconus. *Am J Ophthalmol.* 2020;212:26-33.
102. Ambrosio R, Jr., Belin MW. Imaging of the cornea: topography vs tomography. *J Refract Surg.* 2010;26(11):847-849.
103. Reinstein DZ, Gobbe M, Archer TJ, Silverman RH, Coleman DJ. Epithelial, stromal, and total corneal thickness in keratoconus: three-dimensional display with artemis very-high frequency digital ultrasound. *J Refract Surg.* 2010;26(4):259-271.
104. Salomão MQ, Hofling-Lima AL, Lopes BT, et al. Role of the corneal epithelium measurements in keratorefractive surgery. *Current opinion in ophthalmology.* 2017;28(4):326-336.
105. Li Y, Chamberlain W, Tan O, Brass R, Weiss JL, Huang D. Subclinical keratoconus detection by pattern analysis of corneal and epithelial thickness maps with optical coherence tomography. *J Cataract Refract Surg.* 2016;42(2):284-295.

106. Pahuja N, Shroff R, Pahanpate P, et al. Application of high resolution OCT to evaluate irregularity of Bowman's layer in asymmetric keratoconus. *J Biophotonics.* 2016.
107. Khamar P, Dalal R, Chandapura R, et al. Corneal tomographic features of postrefractive surgery ectasia. *J Biophotonics.* 2019;12(2):e201800253.
108. Ambrosio R, Jr., Nogueira LP, Caldas DL, et al. Evaluation of corneal shape and biomechanics before LASIK. *Int Ophthalmol Clin.* 2011;51(2):11-38.
109. Ambrosio R, Jr., Correia FF, Lopes B, et al. Corneal Biomechanics in Ectatic Diseases: Refractive Surgery Implications. *Open Ophthalmol J.* 2017;11:176-193.
110. Eliasy A, Chen KJ, Vinciguerra R, et al. Determination of Corneal Biomechanical Behavior in-vivo for Healthy Eyes Using CorVis ST Tonometry: Stress-Strain Index. *Front Bioeng Biotechnol.* 2019;7:105.
111. Chong J, Dupps WJ, Jr. Corneal biomechanics: Measurement and structural correlations. *Exp Eye Res.* 2021;205:108508.
112. Scarcelli G, Pineda R, Yun SH. Brillouin optical microscopy for corneal biomechanics. *Invest Ophthalmol Vis Sci.* 2012;53(1):185-190.
113. Scarcelli G, Yun SH. In vivo Brillouin optical microscopy of the human eye. *Opt Express.* 2012;20(8):9197-9202.
114. Shao P, Eltony AM, Seiler TG, et al. Spatially-resolved Brillouin spectroscopy reveals biomechanical abnormalities in mild to advanced keratoconus in vivo. *Sci Rep.* 2019;9(1):7467.
115. Seiler TG, Shao P, Eltony A, Seiler T, Yun SH. Brillouin Spectroscopy of Normal and Keratoconus Corneas. *Am J Ophthalmol.* 2019;202:118-125.
116. Kling S, Akca IB, Chang EW, et al. Numerical model of optical coherence tomographic vibrography imaging to estimate corneal biomechanical properties. *J R Soc Interface.* 2014;11(101):20140920.
117. Kling S, Torres-Netto EA, Spiru B, Sekundo W, Hafezi F. Quasi-Static Optical Coherence Elastography to Characterize Human Corneal Biomechanical Properties. *Invest Ophthalmol Vis Sci.* 2020;61(6):29.
118. Spiru B, Torres-Netto EA, Kling S, Lazaridis A, Hafezi F, Sekundo W. Biomechanical Properties of Human Cornea Tested by Two-Dimensional Extensiometry Ex Vivo in Fellow Eyes: PRK Versus SMILE. *J Refract Surg.* 2019;35(8):501-505.
119. Hosoda Y, Miyake M, Meguro A, et al. Keratoconus-susceptibility gene identification by corneal thickness genome-wide association study and artificial intelligence IBM Watson. *Commun Biol.* 2020;3(1):410.
120. Mas Tur V, MacGregor C, Jayaswal R, O'Brart D, Maycock N. A review of keratoconus: Diagnosis, pathophysiology, and genetics. *Surv Ophthalmol.* 2017;62(6):770-783.
121. Rabinowitz YS, Galvis V, Tello A, Rueda D, Garcia JD. Genetics vs chronic corneal mechanical trauma in the etiology of keratoconus. *Exp Eye Res.* 2021;202:108328.
122. Vinciguerra R, Ambrosio R, Jr., Elsheikh A, et al. Detection of postlaser vision correction ectasia with a new combined biomechanical index. *J Cataract Refract Surg.* 2021;47(10):1314-1318.
123. Flockerzi E, Hafner L, Xanthopoulou K, et al. Reliability analysis of successive Corneal Visualization Scheimpflug Technology measurements in different keratoconus stages. *Acta Ophthalmol.* 2022;100(1):e83-e90.
124. Flockerzi E, Vinciguerra R, Belin MW, Vinciguerra P, Ambrosio R, Jr., Seitz B. Correlation of the Corvis Biomechanical Factor with tomographic parameters in keratoconus. *J Cataract Refract Surg.* 2022;48(2):215-221.
125. Flockerzi E, Vinciguerra R, Belin MW, Vinciguerra P, Ambrosio R, Jr., Seitz B. Combined biomechanical and tomographic keratoconus staging: Adding a biomechanical parameter to the ABCD keratoconus staging system. *Acta Ophthalmol.* 2022;100(5):e1135-e1142.

126. Hashemi H, Heirani M, Ambrósio Jr R, Hafezi F, Naroo SA, Khorrami-Nejad M. The link between Keratoconus and posterior segment parameters: An updated, comprehensive review. *The Ocular Surface.* 2022;23:116-122.
127. Hashemi H, Asgari S, Panahi P, Mehravaran S, Fotouhi A, Ambrósio R. Corneal ectasia in mothers of Down syndrome children. *Scientific reports.* 2021;11(1):1-5.

Legends for Figures:

Figure 1. Basic flow of steps for the data mining and the creation of the AI

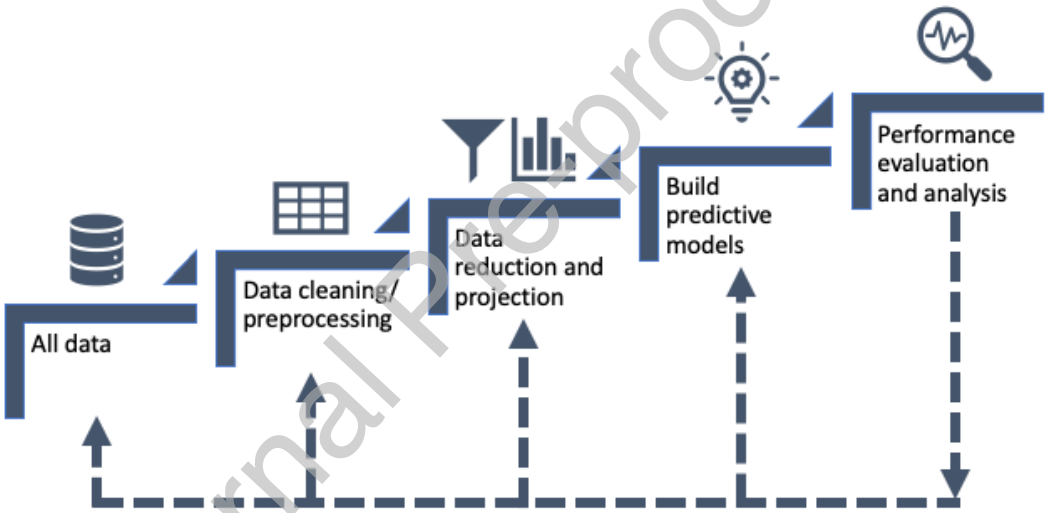

Figure 2. Descriptive statistics for Age

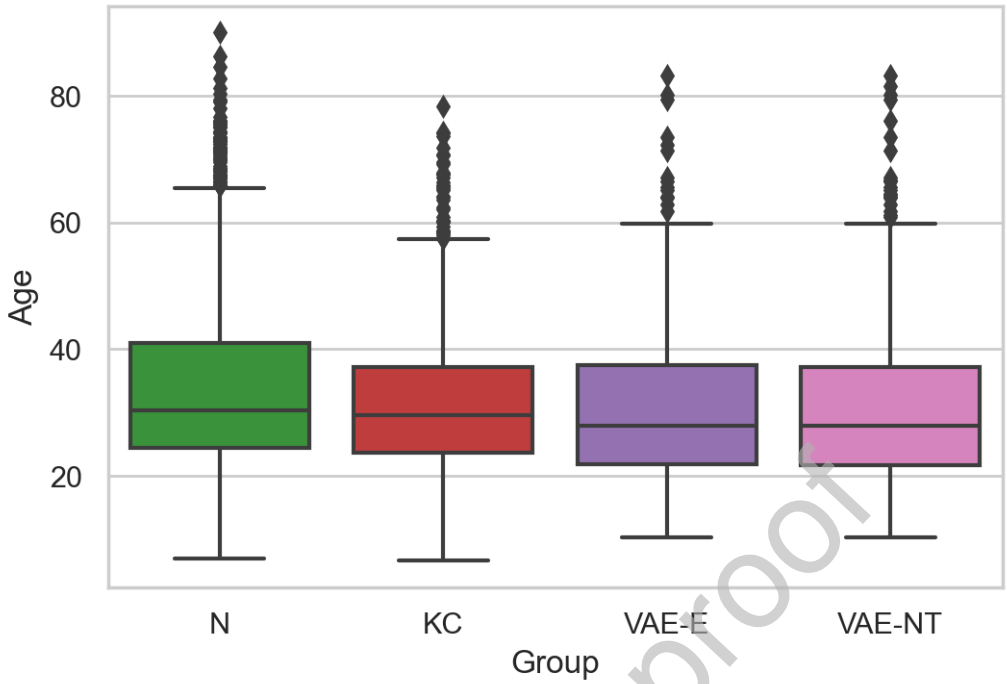

Figure 3. Scatterplot Matrix of the first version of the Tomographic and Biomechanical Index (TBI v.1), the optimized version of the Tomographic and Biomechanical Index (TBI v.2), Pentacam Random Forest Index (PRFI), Corvis Biomechanical Index (CBI), the stiffness parameter at first applanation (SPA1), Belin/Ambrósio Deviation (BAD-D), Belin/Ambrósio Deviation normalized index (BAD-DI) and age.

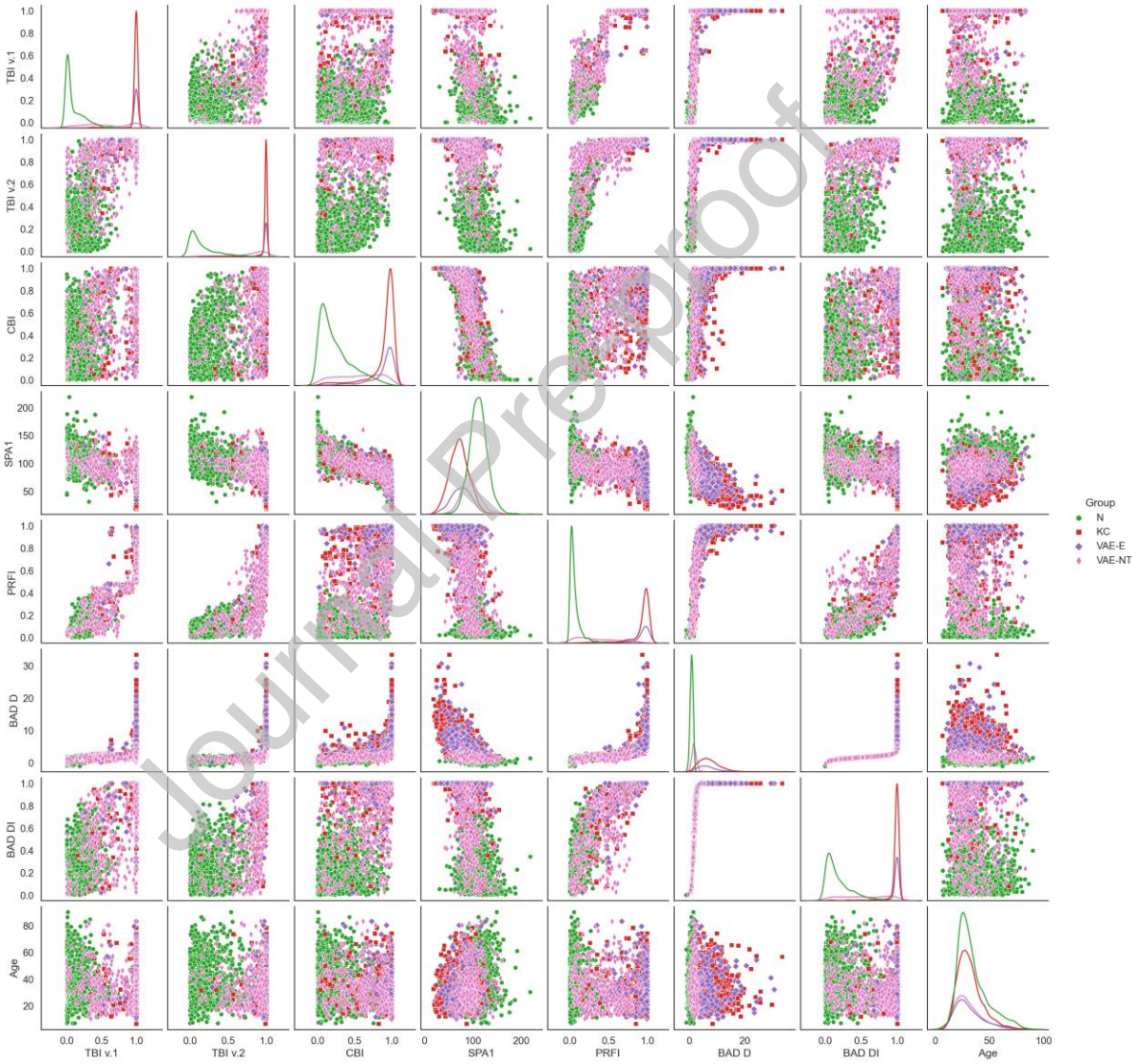

Figure 4. Box and dot plots showing the distribution of metric values across the groups (*n* = 1,680 normal eyes [N], 1,181 keratoconic eyes [KC], 551 eyes with normal topography from very asymmetric ectasia patients [VAE-NT], and 474 ectatic unoperated eyes from the very asymmetric ectasia patients [VAE-E]). (A) The first version of the Tomographic and Biomechanical Index (TBI v.1); (B) The optimized version of the Tomographic and Biomechanical Index (TBI v.2); (C) Pentacam Random Forest Index (PRFI); (D) Corvis Biomechanical Index (CBI); (E) Belin/Ambrósio Deviation (BAD-D); (F) Belin/Ambrósio Deviation normalized index (BAD-DI). The box spans the first and third quartile. The whiskers indicate the 1.5-fold interquartile range. Colored markers representing each value in each patient and its mean are superimposed.

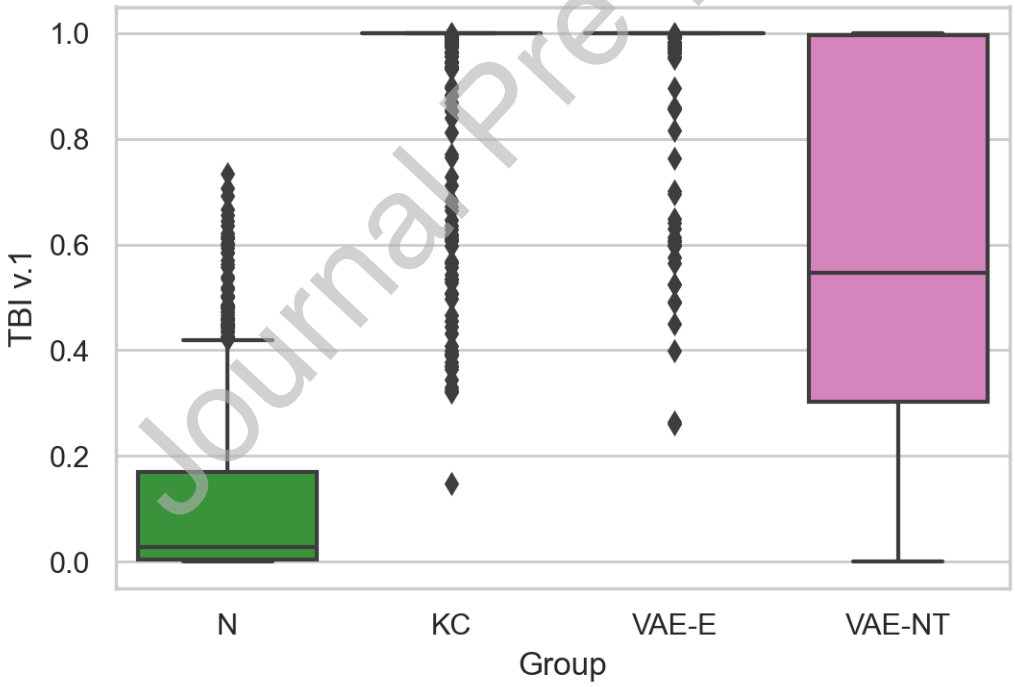

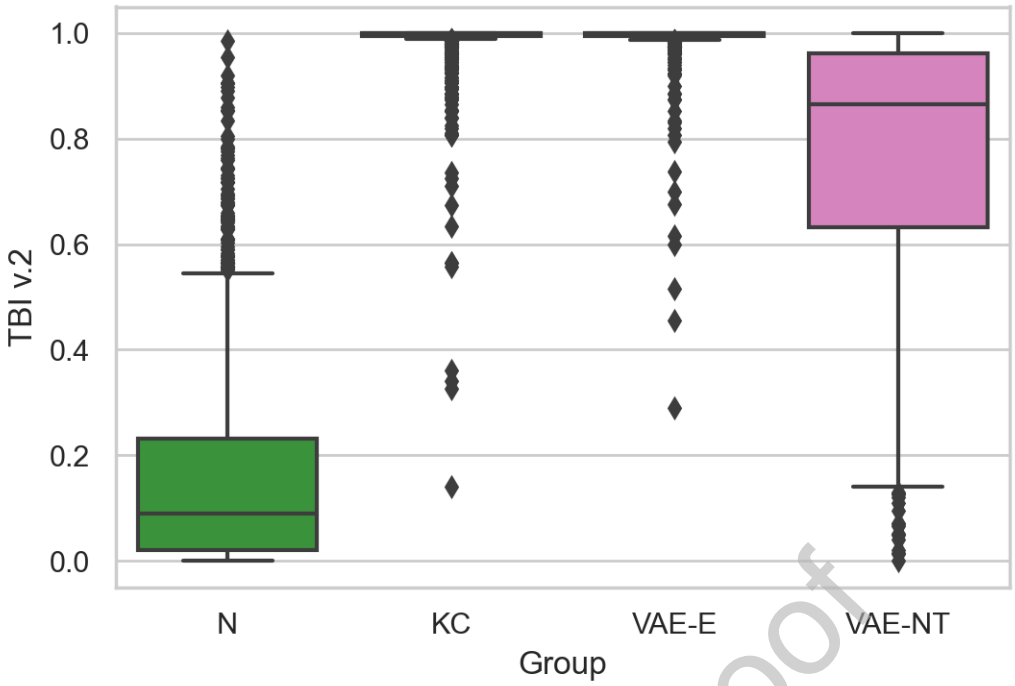

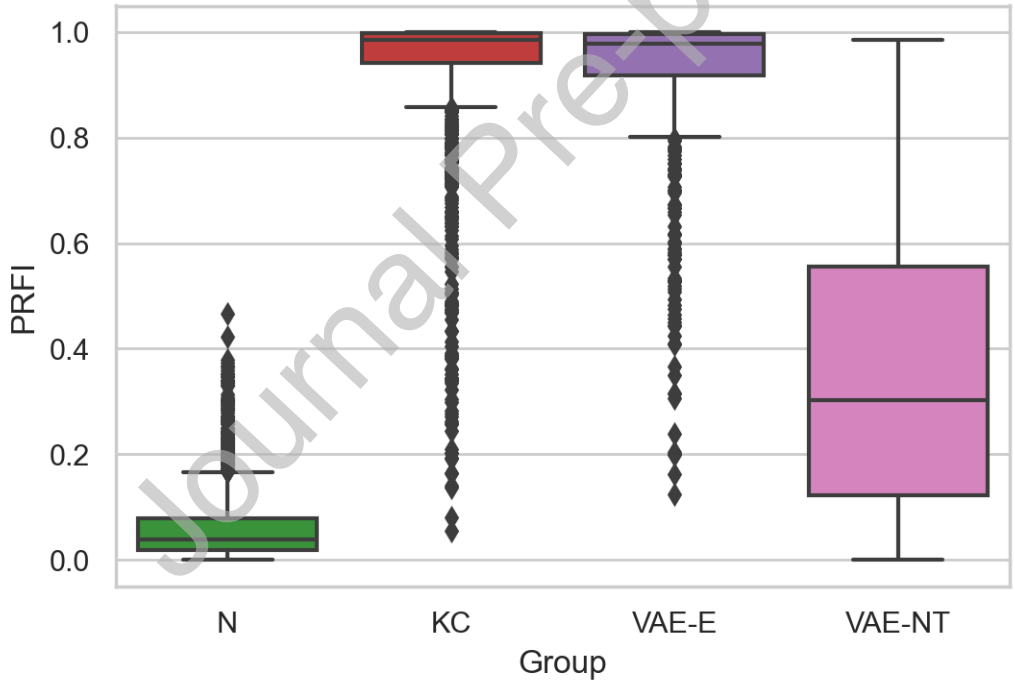

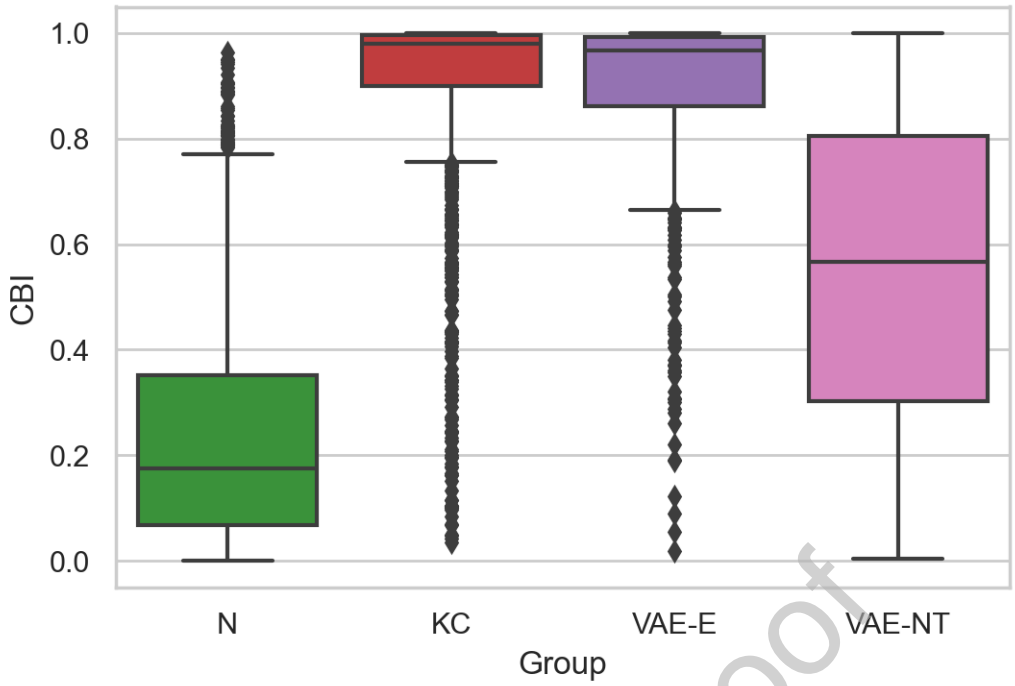

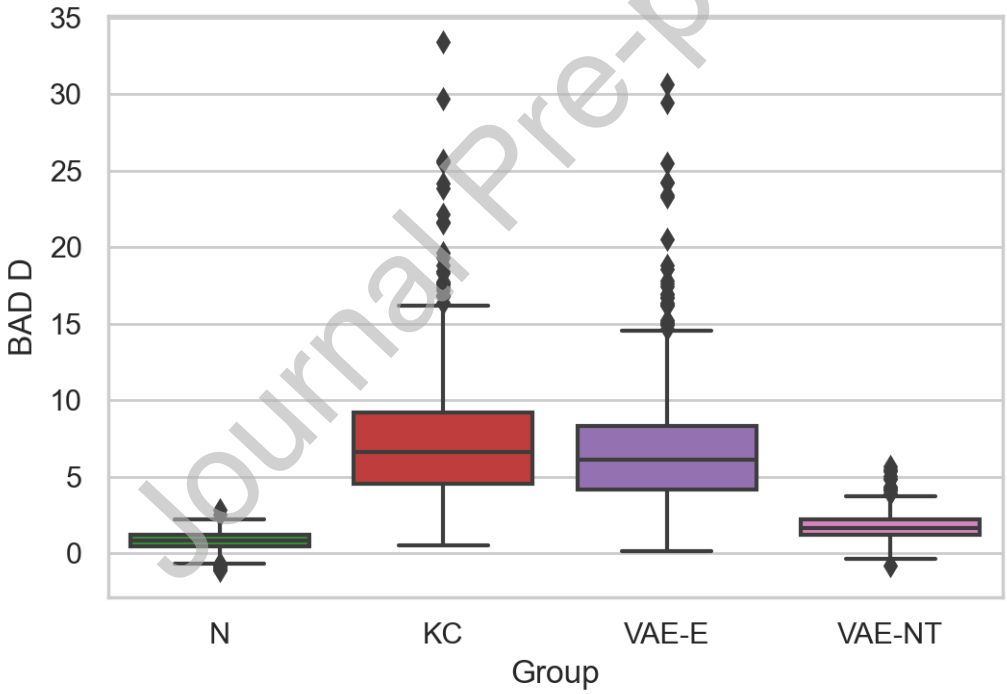

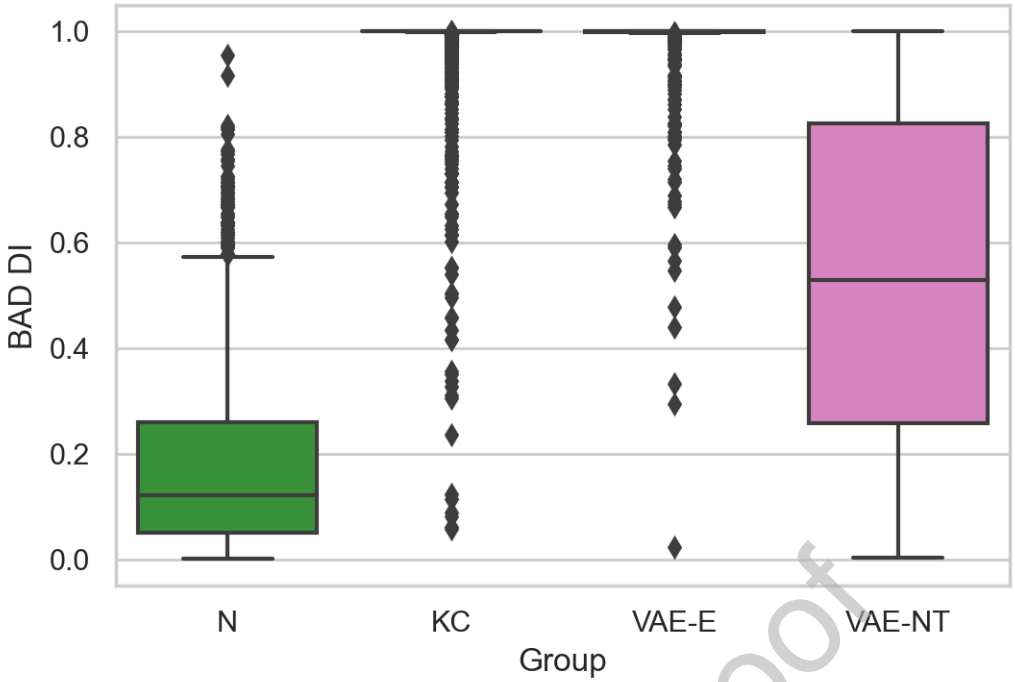

Figure 5. Receiver operating characteristic (ROC) and separation (SEP) curves for the different studies. (A) Normal vs all groups (keratoconus [KC] + very asymmetric ectasia with clinical ectasia (VAE-E) + the normal topography eye from very asymmetric ectasia patients [VAE-NT]); (B) Normal vs clinical ectasia (KC + VAE-E); (C) Normal vs VAE-NT. BAD-D v3 = Belin/Ambrósio (version 3) Deviation; BAD-DI = Belin/Ambrósio Deviation normalized index (BAD-DI); CBI = Corvis Biomechanical Index; PRFI = Pentacam Random Forest Index; TBI = Tomographic and Biomechanical Index

A

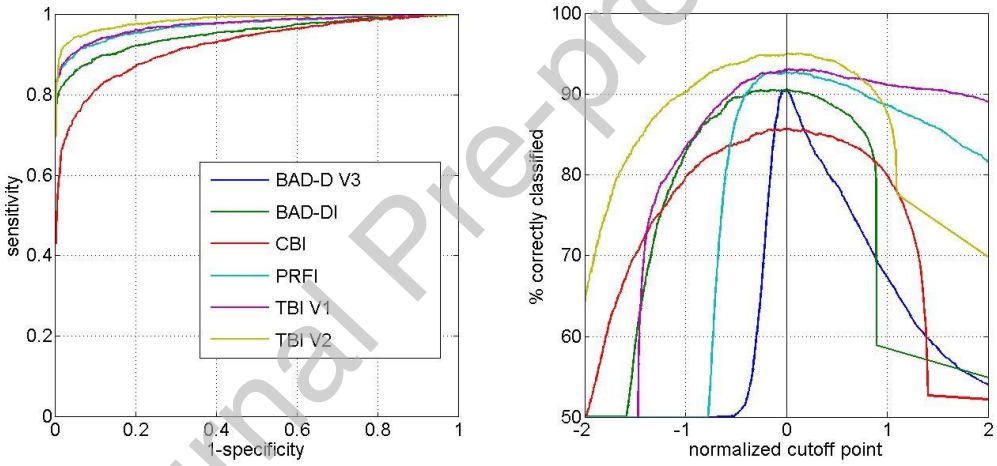

B

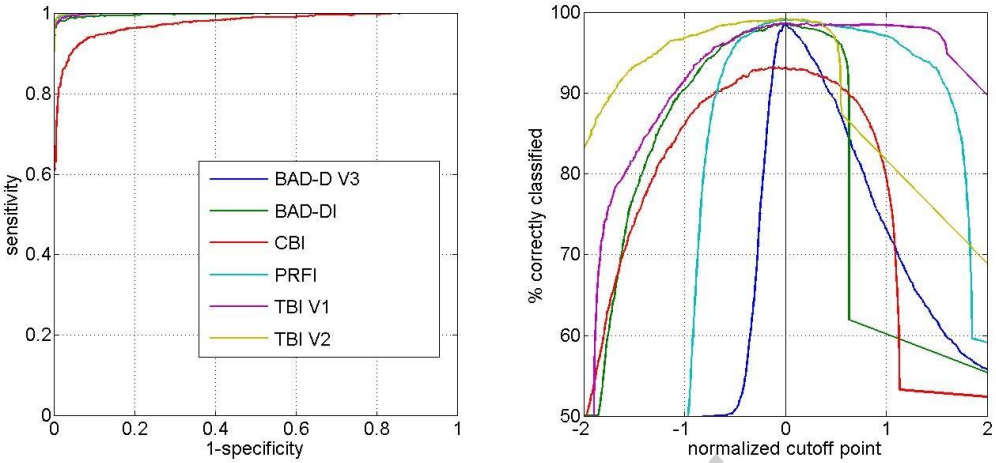

C

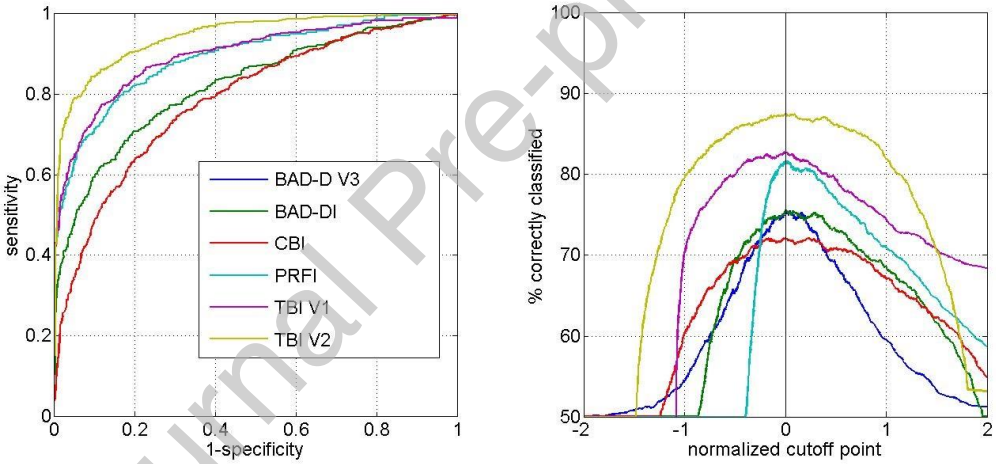

Figure 6. Correlation between the original (TBI v.1) and the optimized version (TBI v.2) of the Tomographic and Biomechanical Index.

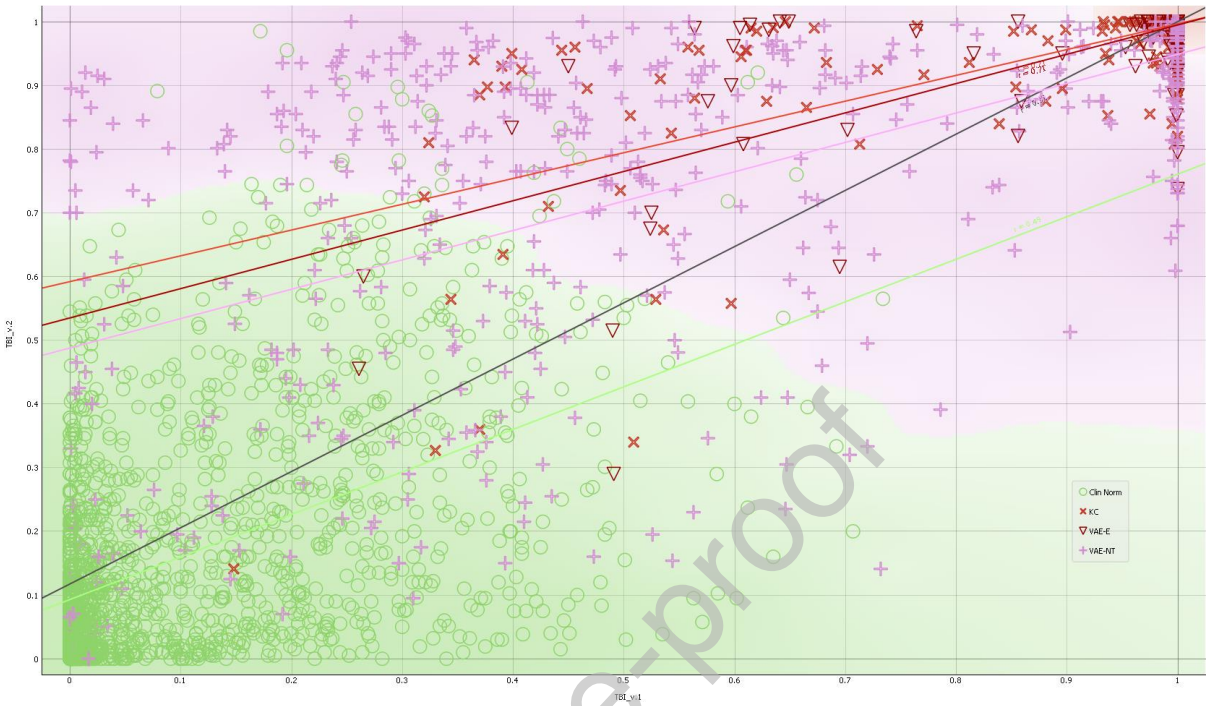

Legends for Tables:

Table 1. Descriptive statistics for Age.

Table 1.

Group	n	Mean	SD	Median	Minimum	25th percentile	75th percentile	Maximum
CLINNORM	1680,00	34,19	13,69	30,37	6,99	24,45	41,00	90,06
KC	1181,00	31,59	11,18	29,59	6,64	23,67	37,18	78,39
VAE-E	474,00	31,03	12,74	27,88	10,34	21,88	37,44	83,15
VAE-NT	551,00	31,02	13,03	27,93	10,34	21,65	37,22	83,15

Table 2. The 18 features selected for the AI algorithm of the TBI v.2.

Table 2.

Parameter	Origin	Parameter
CBI	Corvis ST	Corvis Corneal Biomechanical Index
DARatioTMax2mm	Corvis ST	Ratio of the Deformation Amplityde at 2mm
DensitoIncreaseMax	Corvis ST	Maximal change in backscattering of the cornea from
HC Deformation Amp_mm	Corvis ST	Highest concavity deformation amplitude
MaxInverseRadius	Corvis ST	Minimal Radius of Curvature during concave phase of deformation
PeakDist_mm	Corvis ST	Horizontal distance between the two highest points (nasal and temporal) of the cornea at time of maximum defoormation

SPA1	Corvis ST	Stiffness Parameter at first applanation
SPHC	Corvis ST	Stiffness Parameter at Highest Concavity
BADDb	Pentacam	Deviation from normality of the enhanced posterior elevation best-fit-sphere
BFSFront Thinnest 3mm	Pentacam	Best-fit sphere for anterior 3mm centered at the thinnest point
ISValue	Pentacam	Inferior-Superior Axial Steepening
KMaxFrontY	Pentacam	Vertical Deviation of the point with maximal keratometry (Kmax)from the Apex
Pac_Asymm_ApexVert8.0mm	Pentacam	Vertical Asymmetry of the Pachymetry at 8mm
PRFI	Pentacam	Pentacam Random Forest Index
SphRMin	Pentacam	The minimal mean radius of a ring based on Fourier analysis (zero order component)
TiltMinAxisMVP	Pentacam	Axis location of maximal decentration based on Fourier analysis (first order wave component)
TiltMinMVP	Pentacam	The maximumal decentration based on Fourier analysis (first-order wave component)
Ele. BBFTE 8mm @ Thinnest	Pentacam	Back (posterior) elevation at the thinnest point considering best-fit-toric ellypsoid for 8mm

Table 3. Descriptive of the summarizes the area under the receiver operating characteristic (ROC) and separation (AUSEP) curves calculated between the limits of −1 and +1 standard deviations for (A) Normal vs all groups (keratoconus [KC] + very asymmetric ectasia with clinical ectasia (VAE-E) + the normal topography eye from very asymmetric ectasia patients [VAE-NT]); (B) Normal vs clinical ectasia (KC + VAE-E), and (C) Normal vs VAE-NT. SE=standard error, calculated by Bimonial exact; 95% confidence interval, calculated based on DeLong's method.[59]

Table 3A. Normal x "disease" (KC+VAE-E+VAE-NT)

Variable	AUC	SE [a]	95% CI [b]	AUSEP [c]
TBI_v.1	0.974	0.00236	0.968 to 0.979	82
TBI_v.2	0.985	0.00156	0.981 to 0.989	87
PRFI	0.972	0.00239	0.967 to 0.977	68
BADD	0.952	0.00336	0.945 to 0.959	72
CBI	0.923	0.00418	0.914 to 0.931	68

Table 3B. Normal x "clinical ectasia" (KC+VAE-E)

Variable	AUC	SE [a]	95% CI [b]	AUSEP [c]
TBI_v.1	0.999	0.000269	0.997 to 1.000	93
TBI_v.2	0.999	0.000339	0.997 to 1.000	75
PRFI	0.999	0.000326	0.997 to 1.000	87
BADD	0.995	0.00114	0.992 to 0.997	75
CBI	0.968	0.00283	0.962 to 0.974	81

Table 3C. Normal x "disease" (VAE-NT)

Variable	AUC	SE [a]	95% CI [b]	AUSEP [c]
TBI_v.1	0.899	0.00861	0.886 to 0.911	58
TBI_v.2	0.945	0.00574	0.935 to 0.954	70
PRFI	0.893	0.00862	0.879 to 0.905	36
BADD	0.823	0.0112	0.807 to 0.839	38
CBI	0.788	0.0116	0.771 to 0.805	39

Table 4. Descriptive median, and range (minimum to maximum) for the main parameters: TBIv1 = original Tomographic and Biomechanical Index; TBIv2= optimized version of the Tomographic and Biomechanical Index; PRFI= Pentacam Random Forest Index; BAD-D=Belin/Ambrósio Deviation (version 3); CBI= Corvis Biomechanical Index (CBI), IS-value=the inferior-superior asymmetry at 6mm in diameter; Kmax=maximal keratometric (axial) value on the front surface; ARTmax=Ambrósio's relational thickness to the maximal progression meridian.

Table 4.

	Clin. Normal (n=1.680)			KC (n=1.181)			VAE-E (n=474)			VAE-NT (n=551)		
	Min	**Median**	**Max**	**Min**	**Median**	**Max**	**Min**	**Median**	**Max**	**Min**	**Median**	**Max**
TBI v.1	0	0.028	0.734	0.148	1	1	0.261	1	1	0	0.546	1
TBI v.2	0	0.09	0.985	0.141	1	1	0.29	1	1	0	0.865	1
PRFI	0	0.038	0.466	0.054	0.986	1	0.124	0.978	1	0	0.302	0.986
BADD (v3)	-1.13	0.81	2.81	0.49	6.64	33.42	0.1	6.105	30.63	-0.82	1.64	5.65
CBI	0	0.175	0.964	0.035	0.979	1	0.019	0.967	1	0.003	0.566	1
IS-value (D)	-1.63	0.11	2.16	-2.87	4.66	29.68	-7.08	3.85	19.84	-1.49	0.6	4.3.
K max (D)	39.6	44.5	49.8	41.5	52.3	85.1	42.5	51.6	86.2	38.9	44.7	55.1
ART-max (micra)	267	454	786	0	176	720	0	196	467	126	362	638

Financial Disclosure(s): Dr. Ambrósio, Dr. P. Vinciguerra, Dr. R. Vinciguerra, Dr. Roberts, Dr. B. Lopes, Dr. M. Belin, Dr. A. Ahmed, and Dr. J. Bühren are consultants for Oculus Optikgeräte GmbH (Wetzlar, Germany); The remaining authors have no financial disclosures related to this work.